Article

Structural insights into the inhibition of glycine reuptake

https://doi.org/10.1038/s41586-021-03274-z

Received: 29 May 2020

Accepted: 20 January 2021

Published online: 3 March 2021

Check for updates

Azadeh Shahsavar[1,2], Peter Stohler[3], Gleb Bourenkov[2], Iwan Zimmermann[4,5], Martin Siegrist[3], Wolfgang Guba[3], Emmanuel Pinard[3], Steffen Sinning[6], Markus A. Seeger[4], Thomas R. Schneider[2]✉, Roger J. P. Dawson[3,5]✉ & Poul Nissen[1]✉

The human glycine transporter 1 (GlyT1) regulates glycine-mediated neuronal excitation and inhibition through the sodium- and chloride-dependent reuptake of glycine[1–3]. Inhibition of GlyT1 prolongs neurotransmitter signalling, and has long been a key strategy in the development of therapies for a broad range of disorders of the central nervous system, including schizophrenia and cognitive impairments[4]. Here, using a synthetic single-domain antibody (sybody) and serial synchrotron crystallography, we have determined the structure of GlyT1 in complex with a benzoylpiperazine chemotype inhibitor at 3.4 Å resolution. We find that the inhibitor locks GlyT1 in an inward-open conformation and binds at the intracellular gate of the release pathway, overlapping with the glycine-release site. The inhibitor is likely to reach GlyT1 from the cytoplasmic leaflet of the plasma membrane. Our results define the mechanism of inhibition and enable the rational design of new, clinically efficacious GlyT1 inhibitors.

Glycine is a conditionally essential amino acid with a dual role in the central nervous system (CNS). It acts as a classical neurotransmitter at inhibitory glycinergic synapses, where it induces hyperpolarizing chloride influx at postsynaptic terminals through ionotropic glycine receptors[1,2]. Yet, as the obligatory co-agonist of the *N*-methyl-D-aspartate (NMDA) receptor, glycine also positively modulates calcium-dependent neuronal excitation and plasticity at glutamatergic synapses[1,3]. Glycine homeostasis is tightly regulated by reuptake transporters—including the glycine-specific GlyT1 and GlyT2—that belong to the secondary active neurotransmitter/sodium symporters (NSSs) of the solute carrier 6 (SLC6) transport family[5]. GlyT1 (encoded by the *SLC6A9* gene), GlyT2 (encoded by *SLC6A5*) and the other members of the NSS family, such as the serotonin transporter (SERT), dopamine transporter (DAT) and γ-aminobutyric acid (GABA) transporter (GAT), share a sequence identity of approximately 50%. GlyT1 is located on presynaptic neurons and astrocytes surrounding both inhibitory glycinergic and excitatory glutamatergic synapses, and is considered the main regulator of extracellular levels of glycine in the brain[1,6].

At glutamatergic synapses, GlyT1 has a key role in maintaining subsaturating concentrations of regulatory glycine for the NMDA receptor[7,8]. Hypofunction of the NMDA receptor has been implicated in the pathophysiology of schizophrenia[9], but pharmacological interventions to directly enhance neurotransmission via this receptor in patients with the condition have been unsuccessful[10,11]. Selective inhibition of glycine reuptake by GlyT1 is an alternative approach to increase endogenous extracellular levels of glycine and potentiate NMDA transmission[1,4]. Several chemotypes of potent and selective GlyT1 inhibitors, such as bitopertin, have been developed to achieve antipsychotic and procognitive activity for the treatment of schizophrenia[4,12]. Bitopertin has shown clear signs of enhancing neuroplasticity[13,14] via the glycine-binding site of the NMDA receptor; however, it failed to show efficacy in phase III clinical trials (at a reduced dose), and a drug candidate that targets GlyT1 has yet to emerge.

Studies of NSS and homologues have revealed an alternating-access mechanism[15], which involves a binding and occlusion of the extracellular substrate, dependent on a Na^+ (and Cl^- in eukaryotic NSS) gradient. Binding is followed by a rearrangement to an inward-facing state and subsequent intracellular opening and release of bound ions and substrate. Conformational rearrangements of transmembrane helices during the transport cycle expose the substrate-binding site to either side of the membrane[16–23]. Bitopertin behaves functionally as a non-competitive inhibitor of glycine reuptake[24]; nevertheless, detailed structural information on the inhibitor's binding site, selectivity and underlying molecular mechanism of glycine reuptake inhibition have yet to be obtained. Here we present the structure of human GlyT1 in complex with a highly selective bitopertin analogue[25,26], Cmpd1, and an inhibition-state-selective synthetic nanobody (sybody). Cmpd1 has been patented as a more potent inhibitor targeting GlyT1 that contains a benzoylisoindoline scaffold originating from the bitopertin chemical series[26]. The structure of GlyT1 reveals the molecular determinants and mechanism of action underlying the inhibition of glycine reuptake.

Stabilization and crystal structure of GlyT1

Wild-type human GlyT1 (encoded by *SLC6A9*) is unstable when extracted from the membrane, and contains unstructured termini and a large, flexible extracellular loop 2 (EL2). To enable structure determination, we screened for point mutations that increase thermal stability while preserving ligand-binding activity. For the final crystallization construct, we combined the point mutations L153A,

[1]Danish Research Institute of Translational Neuroscience—DANDRITE, Nordic EMBL Partnership for Molecular Medicine, Department of Molecular Biology and Genetics, Aarhus University, Aarhus, Denmark. [2]European Molecular Biology Laboratory, Hamburg Unit c/o DESY, Hamburg, Germany. [3]Roche Pharma Research and Early Development, Therapeutic Modalities, Roche Innovation Center, Basel, Switzerland. [4]Institute of Medical Microbiology, University of Zurich, Zurich, Switzerland. [5]Linkster Therapeutics AG, Zurich, Switzerland. [6]Department of Forensic Medicine, Aarhus University, Aarhus, Denmark. ✉e-mail: thomas.schneider@embl-hamburg.de; roger.dawson@linkstertherapeutics.com; pn@mbg.au.dk

S297A, I368A and C633A with a shortened EL2 (Δ240–256) and truncated amino and carboxyl termini (Δ1–90 and Δ685–706) (see Methods), and were able to measure persistent transport activity, albeit 42-fold decreased compared with that of wild-type GlyT1 (Extended Data Fig. 1). Adding the selective GlyT1 inhibitor Cmpd1 increases the thermal stability of the transporter further by 30.5 °C (Fig. 1a). Indicative of high-affinity binding with a stabilizing effect, we measured a half-maximal inhibitory concentration (IC_{50}) for Cmpd1 of 12.9 ± 0.9 nM and 7.2 ± 0.4 nM on human and mouse GlyT1, respectively (Fig. 1b), in a membrane-based competition assay with the [^{3}H]Org24598 compound[27] (a non-competitive GlyT1 inhibitor). We therefore purified GlyT1 in the presence of Cmpd1 and generated sybodies to further stabilize the transporter in the inhibition-state conformation, identifying sybody Sb_GlyT1#7 to bind GlyT1 with an affinity of 9 nM (ref. [28]). We then obtained microcrystals of GlyT1 in complex with Sb_GlyT1#7 and Cpmd1 in lipidic cubic phase. Merging the oscillation patterns collected from 409 mounted loops containing microcrystals by a serial synchrotron crystallography approach yielded a complete dataset at 3.4 Å resolution. The structure was determined by molecular replacement using structures of the inward-occluded bacterial multiple hydrophobic amino acid transporter (MhsT; Protein Data Bank identification code (PDB ID) 4US3) and the inward-open human SERT (PDB ID 6DZZ)[17,19]. The high quality of the resulting electron density maps enabled us to unambiguously model human GlyT1 in complex with the sybody and bound ligand (Fig. 1c and Extended Data Fig. 2).

Architecture and conformation of GlyT1

GlyT1 adopts the general architecture of SLC6 transporters, with 12 α-helical transmembrane segments (TMs 1–12) and an inverted pseudo-twofold symmetry that relates two transmembrane domains, TMs 1–5 and 6–10, denoted as the LeuT fold17[18,21,22,29] (Fig. 1c, d). The transporter structure exhibits an inward-open conformation, and superposition of this structure to the inward-open structures of SERT and leucine transporter (LeuT) and inward-oriented occluded MhsT yields Cα root mean square deviations of 1.8 Å, 2.3 Å and 3.2 Å, respectively (see Methods). TM1 and TM6 possess nonhelical segments in the middle of the lipid bilayer; these segments coordinate Na^+ and Cl^- ions[18,20,21], accommodate substrates and inhibitors of various sizes[18,19,22], and stabilize the ligand-free return state[17]. The intracellular part of TM5 is unwound at the conserved helix-breaking Gly(X_9)Pro motif[17] (G313(X_9)P323 in GlyT1), and the N-terminal segment of TM1 (TM1a) is bent away from the core of GlyT1, opening the intracellular pathway to the centre of the transporter (Fig. 2a). The splayed motion of TM1 disrupts the interaction between the conserved residues W103 of TM1a and Y385 at the cytoplasmic part of TM6 that is otherwise present in outward-open and occluded conformations[17,18,20,22] (Extended Data Fig. 3 and Supplementary Fig. 1).

Comparison of GlyT1 with inward-open SERT shows structural differences mainly at the intracellular halves of the helices (Extended Data Fig. 4a–e), and in particular at the intracellular gate of GlyT1 defined by TM1a and TM5. The intracellular half of TM5 has splayed away from the transporter core by 17°, whereas TM1a is by 29° closer, compared with corresponding segments of SERT. As a result, the intracellular gate—measured as the Cα–Cα distance between the conserved W103 on TM1a and V315 on TM5—is by 4 Å more closed than that of the inward-open structure of ibogaine-bound SERT (Extended Data Fig. 4b, e). On the extracellular side, a Cα–Cα distance of 8.9 Å between R125 of TM1a and D528 of TM10, and a close packing of the extracellular vestibule around W124 in the NSS-conserved NVWRFPY motif of TM1, indicates a closed extracellular gate (Fig. 2a, Extended Data Fig. 3 and Supplementary Fig. 1).

The conformation-specific sybody binds through several interactions to the extracellular segment of GlyT1, involving EL2, EL4, TM5 and TM7 (Fig. 1c and Extended Data Fig. 5a). Sb_GlyT1#7 is selective for the

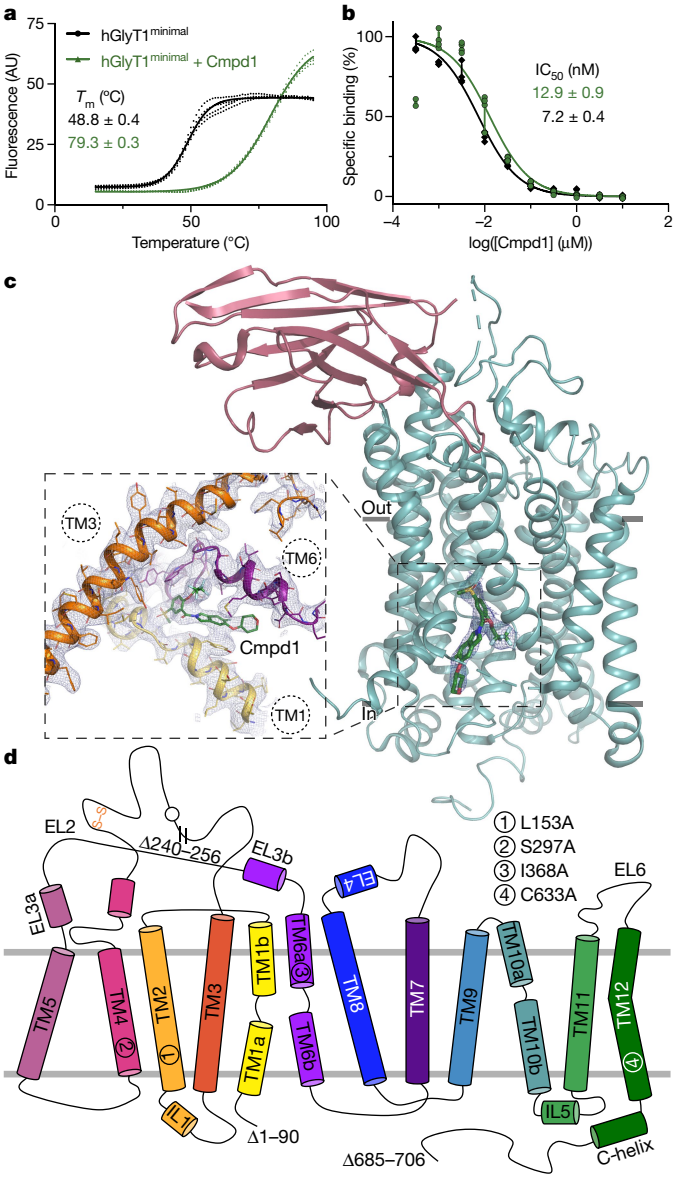

Fig. 1 | Stabilization, binding and recognition of inhibitor Cmpd1 by human GlyT1. a, Increasing concentrations of Cmpd1 show a strong dose-dependent stabilization of GlyT1, raising the melting point from 48.8 ± 0.4 °C to 79.3 ± 0.3 °C (mean ± s.e.m.). Data for GlyT1^{minimal} (containing deletions of the N and C termini) with and without addition of the inhibitor are depicted in green and black, respectively. Individual data points from $n = 4$ technical replicates are shown. AU, arbitrary units. **b**, Cmpd1 inhibits mouse and human GlyT1 with an IC_{50} of 7.2 ± 0.4 nM and 12.9 ± 0.9 nM (mean ± s.e.m.), respectively, in membrane-based competition assays with [^{3}H]Org24598. Curves were calculated from $n = 4$ technical replicates (individual data points are shown; whiskers extend from minimum to maximum). **c**, Overall structure of human GlyT1 bound to the selective inhibitor Cmpd1 and an inhibition-state-selective sybody. A magnified view of the inhibitor-binding pocket in a $2F_o - F_c$ electron density map (blue mesh) countered at 1.0 r.m.s.d. is depicted. TM8 is not shown for clarity. **d**, Topology diagram of the GlyT1 crystallization construct. EL2 carries a strictly conserved disulfide bridge (C220–C229) and four *N*-linked glycosylation sites, N237, N240, N250 and N256. Three glycosylation sites were removed by the EL2 truncation (240–256), but N237 was essential for membrane-based ligand binding, probably enabling correct trafficking of the transporter to the plasma membrane[40]. The one remaining glycosylation site at N237 is shown as a sphere on EL2. The locations of the single point mutations L153A, S297A, I368A and C633A on transmembrane helices are shown.

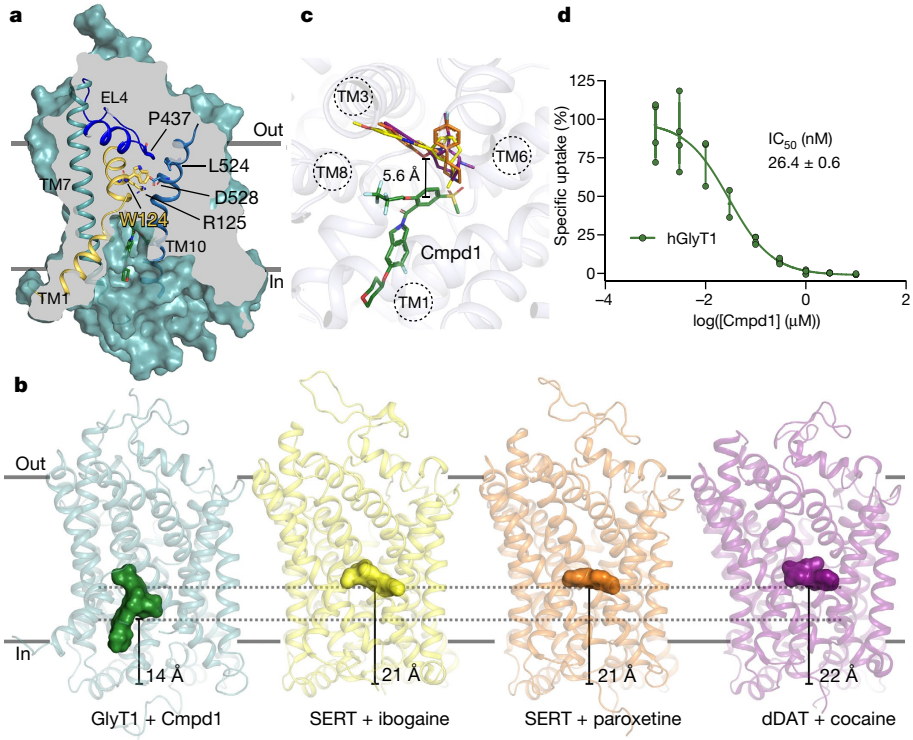

Fig. 2 | Inhibition of glycine uptake and binding mode of Cmpd1 at inward-open GlyT1. a, Surface representation of the inward-open structure of GlyT1, viewed parallel to the membrane. The closed extracellular vestibule around W124 (yellow) and the open intracellular pathway are displayed. Residues R125 (TM1), P437 (EL4), L524 and D528 (TM10) are shown as sticks. **b**, **c**, Comparison of the binding modes of Cmpd1 (green) in GlyT1 with the inhibitor-binding sites in other NSS transporters. Paroxetine (orange) and ibogaine (yellow) bound to SERT (PDB IDs 5I6X and 6DZY, respectively) and cocaine (purple) bound to *Drosophila melanogaster* DAT (dDAT, PDB ID 4XP4) are shown as examples. The differences in the locations of the bound ligands in the transporters are marked with dotted lines in **b**. Compared with paroxetine, ibogaine and cocaine, Cmpd1 is located 5.6 ± 0.1 Å further away from the centre of the transporter (shown in **c**). This distance is measured between the centre of the phenyl ring of Cmpd1 and the centre of mass of the other NSS inhibitors shown. **d**, Cmpd1 inhibits the uptake of glycine by human GlyT1 with an IC_{50} of 26.4 ± 0.6 nM (mean ± s.e.m.). The curve was calculated from $n = 4$ technical replicates (individual data points are shown; whiskers extend from minimum to maximum).

inward-open conformation of GlyT1 and has a conformation-stabilizing effect, as shown by an increase of 10 °C in thermal stability and an apparent affinity increase for [^{3}H]Org24598 of almost twofold in a scintillation proximity assay[28]. In addition to stabilizing the inhibition state, the sybody takes a central role in forming the lattice contacts, packing against the neighbouring sybody in the crystal (Extended Data Fig. 5d).

Unique binding mode among NSS transporters

An unambiguous electron density for the inhibitor Cmpd1 was observed in proximity to the central binding pocket of GlyT1, between transmembrane helices 1, 3, 6 and 8 (Fig. 1c and Extended Data Fig. 5b). Comparison of the inhibitor-binding site in GlyT1 with the equivalent site of other NSS structures shows that Cmpd1 is within 6.0 ± 0.5 Å of the core, with its centre of mass located 14 Å from the cytosolic face of the transporter, while inhibitors of SERT and DAT bind at the central binding site within 21–22 Å of the cytosolic face (Fig. 2b, c). Furthermore, the inhibitor binds GlyT1 in a unique binding mode, lodged in proximity to the centre of the transporter and extending into the intracellular release pathway for substrate and ions between TM6b and TM1a, accessible to solvent. This mode of inhibition is not observed in other NSS–inhibitor complexes (Fig. 2b, c).

Cmpd1 is from the benzoylisoindoline class of selective GlyT1 inhibitors[25], and inhibits the uptake of glycine in mammalian cells (Flp-in-CHO cells) expressing mouse[26] or human GlyT1 with an IC_{50} of 7.0 ± 0.4 nM and 26.4 ± 0.6 nM, respectively (Fig. 2d). The isoindoline scaffold of Cmpd1 forms a π-stacking interaction with Y116 of TM1. The phenyl ring is engaged in an edge-to-face stacking interaction with the aromatic ring of W376 located on the unwound region of TM6. The inhibitor is further stabilized by hydrogen-bond and van der Waals interactions with residues from TM1, TM3, TM6 and TM8 (Fig. 3a and Extended Data Figs. 5c, 6a, b).

We generated a stable construct with a single point mutation, I192A, that was not able to bind the inhibitor. Notably, I192 is within van der Waals distance of the W376 side chain, which is stabilized in a rotamer perpendicular to the phenyl ring of the inhibitor (Extended Data Fig. 6c–e). W376 is the bulky hydrophobic residue of a conserved (G/A/C)ΦG motif in the unwound segment of TM6 that determines the substrate selectivity of SLC6 transporters[30–32], and the AWG sequence observed in GlyT1 is indeed fitting for a small glycine substrate. I192, although not in direct interaction with the inhibitor, plays an important part in the binding of Cmpd1 by reducing the rotational freedom of the W376 side chain, which may also further restrict the binding pocket for glycine.

Adding a lichenase fusion protein construct[33] (PDB ID 2CIT) to the N terminus of the GlyT1 construct, we generated and crystallized a GlyT1–Lic fusion protein in complex with Sb_GlyT1#7, and obtained a dataset at 3.9 Å resolution collected from 1,222 mounted loops containing microcrystals (Extended Data Fig. 5d). The electrogenic reuptake of glycine via GlyT1 is coupled to the transport of two Na^+ and one Cl^- ions. Both the GlyT1 and the GlyT1–Lic constructs were purified and crystallized in the presence of 150 mM NaCl and adopt the same inward-open, inhibitor-bound conformation. However, we observe electron density for Na^+ and Cl^- ions only in the lower-resolution map of the GlyT1–Lic crystal structure, which may have captured a preceding state

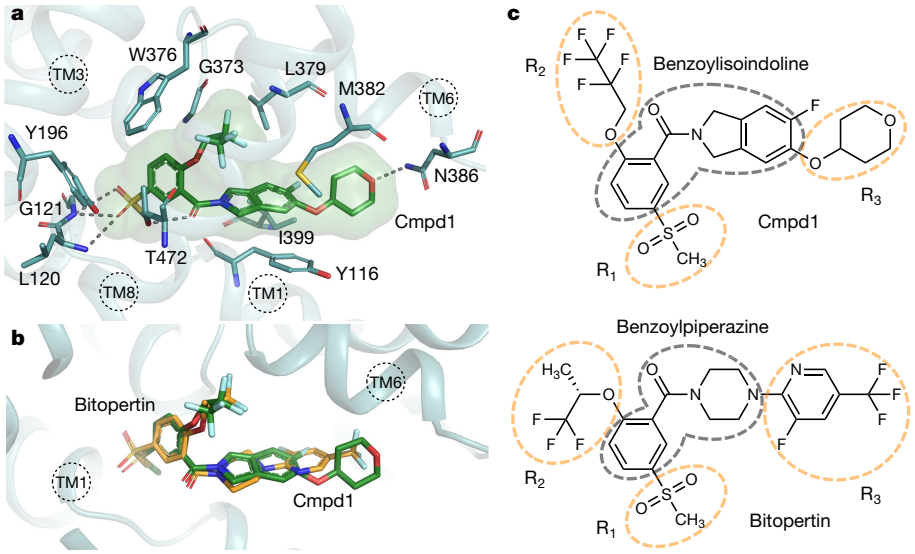

Fig. 3 | Binding pocket. a, Close-up view of the Cmpd1-binding pocket in GlyT1. The two ends of the inhibitor are stabilized by hydrogen-bond interactions with residues from TM1 and TM6; the backbone amine groups of G121 and L120 form hydrogen bonds with sulfonyl oxygen atoms, and N386 from TM6 forms a hydrogen bond with the oxygen atom of the tetrahydropyran moiety of the inhibitor. From TM8, the hydroxyl group of T472 participates in a hydrogen-bonding interaction with the carbonyl oxygen of the scaffold. The aromatic ring of Y116, localized 4.2 Å from the isoindoline scaffold of the compound (a π-stacking interaction), is shown. The hydroxyl group of Y196 from TM3 probably forms a weaker hydrogen-bond interaction with the methyl sulfone moiety of the inhibitor. Inhibitor binding is also supported by an edge-to-face stacking interaction between the phenyl ring of the ligand and the aromatic sidechain of W376. The residues that form the binding pocket, G373, L379 and M382 (TM6) and I399 (TM7), are also depicted. **b**, Docking of bitopertin (orange) into the inhibitor-binding pocket of GlyT1, comparing the binding modes of bitopertin and Cmpd1 (green). **c**, Comparison of Cmpd1 (benzoylisoindoline series, top) and bitopertin (benzoylpiperazine series, bottom). The scaffolds of the compounds are marked with grey dashed lines, and the three R groups are marked with orange dashed lines.

in transitions associated with ion release to the intracellular environment (Extended Data Fig. 7a, b).

Plasticity of the binding pocket

Similar to reported benzoylisoindolines[25], Cmpd1 is more than 1,000-fold selective for GlyT1 against GlyT2 (Extended Data Fig. 6f). Comparing the binding-pocket residues of GlyT1 with corresponding residues in GlyT2 points to direct clues. G373 in GlyT1 corresponds to S497 in GlyT2. Notably, *N*-methyl glycine (sarcosine) and *N*-ethyl glycine are substrates of GlyT1 and the S497G mutant of GlyT2, but not of wild-type GlyT2[31,34,35], which can be explained readily by a steric clash with S497. Furthermore, GlyT1 residues M382 and I399 correspond to leucine and valine, respectively, in GlyT2; the latter two diminish the van der Waals interactions between the inhibitor and the transporter.

Molecular docking places bitopertin in the binding pocket of GlyT1, with its benzoylpiperazine scaffold matching the benzoylisoindoline scaffold of Cmpd1 (Fig. 3b). The binding mode and scaffold substituent interactions (R_1–R_3) are supported by the previously reported structure–activity relationships of the benzoylpiperazine and benzoylisoindoline series[12,25]. The R_1 pocket (hosting a methyl sulfone moiety) is spatially constrained and prefers small, polar substituents with a hydrogen-bond-acceptor group. The pocket harbouring R_2 substituents (O–C_3F_5) is mainly hydrophobic and accommodates linear and cyclic substituents up to a ring size of six. The R_3 (tetrahydropyran) pocket is fairly large and exposed to solvent, and can accommodate diverse groups with different functionalities (Fig. 3c). We observed a higher flexibility for the tetrahydropyran moiety, as the corresponding portion of the electron density was not well resolved. Considering the size and solvent exposure of this pocket, the R_3 position is the favourable handle to fine-tune the physicochemical properties of the inhibitor.

Superposition of glycine-bound LeuT and tryptophan-bound MhsT on inhibitor-bound GlyT1 shows that the sulfonyl moiety of the inhibitor probably mimics the carboxylate group of the glycine substrate, interacting with TM1 and TM3 (Extended Data Fig. 7c, d). We observe that at a glycine concentration of more than 0.1 mM, selective inhibitors of GlyT1 are outcompeted, further supporting the existence of overlapping binding sites (Extended Data Fig. 7e).

Mechanism of inhibition

Although GlyT1's binding site for bitopertin and Cmpd1 appears to overlap with its glycine-binding site, these are not competitive glycine-reuptake inhibitors[4,24] (Extended Data Figs. 7c–e, 8). It is likely that, owing to their hydrophobic nature[12,25], Cmpd1, bitopertin and related chemotypes diffuse across the cell membrane and bind from the cytoplasmic side to an inward-open structure, involving unwinding of the TM5 segment and a hinge-like motion of TM1a to fit the bulky inhibitor (Fig. 4). Glycine, on the other hand, binds to the outward-open conformation, which is exposed to high concentrations of the driving Na^+ and Cl^- ions at the synaptic environment. Following binding of glycine and ions, the transporter transforms to an inward-open conformation with low affinity for glycine, and this is where direct binding competition can occur, with the inhibitor having a high affinity for the site.

Release of ions and glycine from the inward-open state enables bitopertin, Cmpd1 and similar transport inhibitors to bind and shift the conformational equilibrium towards an inward-open conformation. As with the inhibition of inward-open SERT by ibogaine[36], the binding sites of glycine and non-competitive inhibitors of GlyT1 explore two distinct conformational states, outward and inward oriented (Fig. 4).

Considering the high membrane permeability measured for Cmpd1 and bitopertin[12,25], it is likely that the inhibitor dissipates into locations other than the synapse. In fact, GlyT1 is also expressed in peripheral tissues, including erythrocytes where glycine plays a key part in the biosynthesis of haem. Inhibition of GlyT1 by bitopertin in these cells results in a tolerable decrease in the level of haemoglobin. However, the possible risks associated with such an effect were a prohibitory factor in phase III clinical trials of bitopertin, which was therefore administered

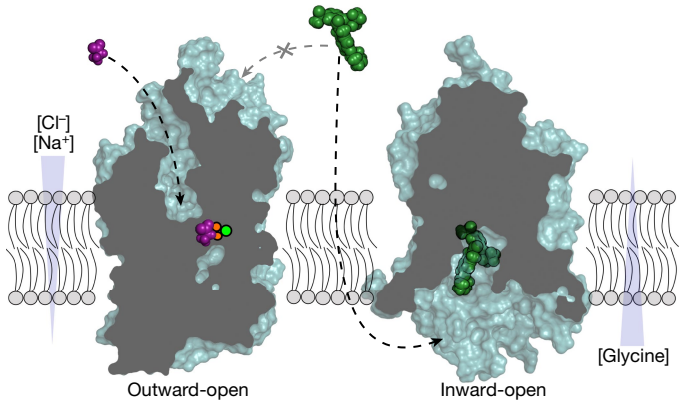

Fig. 4 | Mechanism of inhibition of GlyT1. Left, glycine (purple) binds with high affinity to the outward-open conformation of GlyT1 (homology model based on dDAT, PDB ID 4M48), which is exposed to high concentrations of the driving Na^+ and Cl^- ions (orange and green spheres, respectively) in the synaptic environment. Right, the inhibitor Cmpd1 (green) can diffuse across the synaptic cell membrane and reach the intracellular side of GlyT1. Cmpd1 locks the transporter in an inward-open conformation, with the characteristic hinge-like motion of TM1a and unwinding of TM5. Cmpd1 inhibits GlyT1 by shifting the conformational equilibrium to the inward-open state.

at a lower dose than in the proof-of-concept phase II clinical studies. It also remains unclear whether administration of bitopertin reached optimal GlyT1 occupancy in trial subjects, or whether a higher placebo response in clinical trials resulted in an indistinguishable efficacy of bitopertin[10,37,38].

The sybody Sb_GlyT1#7 is also highly selective for the inhibited, inward-open conformation of GlyT1. Recent efforts to engineer antibodies that achieve effective targeting and efficient crossing of the blood–brain barrier[39] to deliver an inhibition-state-specific sybody represent an alternative approach to small-molecule inhibitors of GlyT1. The structure of human GlyT1 presented here provides a platform for the rational design of new small-molecule inhibitors and antibodies that target the glycine-reuptake transporter.

Online content

Any methods, additional references, Nature Research reporting summaries, source data, extended data, supplementary information, acknowledgements, peer review information; details of author contributions and competing interests; and statements of data and code availability are available at https://doi.org/10.1038/s41586-021-03274-z.

1. Harvey, R. J. & Yee, B. K. Glycine transporters as novel therapeutic targets in schizophrenia, alcohol dependence and pain. *Nat. Rev. Drug Discov.* **12**, 866–885 (2013).
2. Grenningloh, G. et al. The strychnine-binding subunit of the glycine receptor shows homology with nicotinic acetylcholine receptors. *Nature* **328**, 215–220 (1987).
3. Johnson, J. W. & Ascher, P. Glycine potentiates the NMDA response in cultured mouse brain neurons. *Nature* **325**, 529–531 (1987).
4. Cioffi, C. L. Glycine transporter-1 inhibitors: a patent review (2011–2016). *Expert Opin. Ther. Pat.* **28**, 197–210 (2018).
5. Kristensen, A. S. et al. SLC6 neurotransmitter transporters: structure, function, and regulation. *Pharmacol. Rev.* **63**, 585–640 (2011).
6. Gomeza, J. et al. Inactivation of the glycine transporter 1 gene discloses vital role of glial glycine uptake in glycinergic inhibition. *Neuron* **40**, 785–796 (2003).
7. Cubelos, B., Giménez, C. & Zafra, F. Localization of the GLYT1 glycine transporter at glutamatergic synapses in the rat brain. *Cereb. Cortex* **15**, 448–459 (2005).
8. Cubelos, B., González-González, I. M., Giménez, C. & Zafra, F. The scaffolding protein PSD-95 interacts with the glycine transporter GLYT1 and impairs its internalization. *J. Neurochem.* **95**, 1047–1058 (2005).
9. Kantrowitz, J. T. & Javitt, D. C. *N*-methyl-D-aspartate (NMDA) receptor dysfunction or dysregulation: the final common pathway on the road to schizophrenia? *Brain Res. Bull.* **83**, 108–121 (2010).
10. Pinard, E., Borroni, E., Koerner, A., Umbricht, D. & Alberati, D. Glycine transporter type I (GlyT1) inhibitor, bitopertin: a journey from lab to patient. *CHIMIA Int. J. Chem.* **72**, 477–484 (2018).
11. Shim, S. S., Hammonds, M. D. & Kee, B. S. Potentiation of the NMDA receptor in the treatment of schizophrenia: focused on the glycine site. *Eur. Arch. Psychiatry Clin. Neurosci.* **258**, 16–27 (2007).
12. Pinard, E. et al. Selective GlyT1 inhibitors: discovery of [4-(3-fluoro-5-trifluoromethylpyridin-2-yl)piperazin-1-yl][5-methanesulfonyl-2-((S)-2,2,2-trifluoro-1-methylethoxy)phenyl]methanone (RG1678), a promising novel medicine to treat schizophrenia. *J. Med. Chem.* **53**, 4603–4614 (2010).
13. Krystal, J. H. et al. Neuroplasticity as a target for the pharmacotherapy of anxiety disorders, mood disorders, and schizophrenia. *Drug Discov. Today* **14**, 690–697 (2009).
14. D'Souza, D. C. et al. Dose-related target occupancy and effects on circuitry, behavior, and neuroplasticity of the glycine transporter-1 inhibitor PF-03463275 in healthy and schizophrenia subjects. *Biol. Psychiatry* **84**, 413–421 (2018).
15. Jardetzky, O. Simple allosteric model for membrane pumps. *Nature* **211**, 969–970 (1966).
16. Kazmier, K. et al. Conformational dynamics of ligand-dependent alternating access in LeuT. *Nat. Struct. Mol. Biol.* **21**, 472–479 (2014).
17. Malinauskaite, L. et al. A mechanism for intracellular release of Na^+ by neurotransmitter/sodium symporters. *Nat. Struct. Mol. Biol.* **21**, 1006–1012 (2014).
18. Penmatsa, A., Wang, K. H. & Gouaux, E. X-ray structure of dopamine transporter elucidates antidepressant mechanism. *Nature* **503**, 85–90 (2013).
19. Coleman, J. A. et al. Serotonin transporter–ibogaine complexes illuminate mechanisms of inhibition and transport. *Nature* **569**, 141–145 (2019).
20. Gotfryd, K. et al. X-ray structure of LeuT in an inward-facing occluded conformation reveals mechanism of substrate release. *Nat. Commun.* **11**, 1005 (2020).
21. Singh, S. K., Yamashita, A. & Gouaux, E. Antidepressant binding site in a bacterial homologue of neurotransmitter transporters. *Nature* **448**, 952–956 (2007).
22. Coleman, J. A., Green, E. M. & Gouaux, E. X-ray structures and mechanism of the human serotonin transporter. *Nature* **532**, 334–339 (2016).
23. Malinauskaite, L. et al. A conserved leucine occupies the empty substrate site of LeuT in the Na^+-free return state. *Nat. Commun.* **7**, 11673 (2016).
24. Alberati, D. et al. Glycine reuptake inhibitor RG1678: a pharmacologic characterization of an investigational agent for the treatment of schizophrenia. *Neuropharmacology* **62**, 1152–1161 (2012).
25. Pinard, E. et al. Discovery of benzoylisoindolines as a novel class of potent, selective and orally active GlyT1 inhibitors. *Bioorg. Med. Chem. Lett.* **20**, 6960–6965 (2010).
26. Jolidon, S., Narquizian, R., Norcross, R. D. & Pinard, E. Heterocyclic substituted phenyl methanones as inhibitors of the glycine transporter 1. WIPO patent WO/2006/082001 (2006).
27. Brown, A. et al. Discovery and SAR of Org 24598—a selective glycine uptake inhibitor. *Bioorg. Med. Chem. Lett.* **11**, 2007–2009 (2001).
28. Zimmermann, I. et al. Synthetic single domain antibodies for the conformational trapping of membrane proteins. *eLife* **7**, e34317 (2018).
29. Abramson, J. & Wright, E. M. Structure and function of Na^+-symporters with inverted repeats. *Curr. Opin. Struct. Biol.* **19**, 425–432 (2009).
30. LeVine, M. V. et al. The allosteric mechanism of substrate-specific transport in SLC6 is mediated by a volumetric sensor. *Proc. Natl Acad. Sci. USA* **116**, 15947–15956 (2019).
31. Carland, J. E. et al. Molecular determinants for substrate interactions with the glycine transporter GlyT2. *ACS Chem. Neurosci.* **9**, 603–614 (2018).
32. Focht, D. et al. A non-helical region in transmembrane helix 6 of hydrophobic amino acid transporter MhsT mediates substrate recognition. *EMBO J.* **40**, e105164 (2020).
33. Jaeger, K. et al. Structural basis for allosteric ligand recognition in the human CC chemokine receptor 7. *Cell* **178**, 1222–1230 (2019).
34. Vandenberg, R. J., Shaddick, K. & Ju, P. Molecular basis for substrate discrimination by glycine transporters. *J. Biol. Chem.* **282**, 14447–14453 (2007).
35. Werdehausen, R. et al. Lidocaine metabolites inhibit glycine transporter 1: a novel mechanism for the analgesic action of systemic lidocaine? *Anesthesiology* **116**, 147–158 (2012).
36. Jacobs, M. T., Zhang, Y.-W., Campbell, S. D. & Rudnick, G. Ibogaine, a noncompetitive inhibitor of serotonin transport, acts by stabilizing the cytoplasm-facing state of the transporter. *J. Biol. Chem.* **282**, 29441–29447 (2007).
37. Bugarski-Kirola, D. et al. Bitopertin in negative symptoms of schizophrenia-results from the phase III FlashLyte and DayLyte studies. *Biol. Psychiatry* **82**, 8–16 (2017).
38. Martin-Facklam, M. et al. Glycine transporter type 1 occupancy by bitopertin: a positron emission tomography study in healthy volunteers. *Neuropsychopharmacology* **38**, 504–512 (2013).
39. Weber, F. et al. Brain shuttle antibody for Alzheimer's disease with attenuated peripheral effector function due to an inverted binding mode. *Cell Rep.* **22**, 149–162 (2018).
40. Olivares, L., Aragón, C., Giménez, C. & Zafra, F. The role of *N*-glycosylation in the targeting and activity of the GLYT1 glycine transporter. *J. Biol. Chem.* **270**, 9437–9442 (1995).
41. Gati, C. et al. Serial crystallography on in vivo grown microcrystals using synchrotron radiation. *IUCrJ.* **1**, 87–94 (2014).

Methods

No statistical methods were used to predetermine sample size. The experiments were not randomized, and investigators were not blinded to allocation during experiments and outcome assessment.

GlyT1 constructs

The human GlyT1 complementary DNA sequence was codon optimized and synthesized by Genewiz for expression in mammalian cells, and the GlyT1–Lic sequence for insect cell expression. Both constructs contain N- and C-terminal deletions of residues 1–90 and 685–706, respectively (minimal construct GlyT1^{minimal}) as well as a deletion in the extracellular loop 2 (EL2) between residues 240 and 256. To improve the thermal stability of the constructs, we introduced single point mutations to the transmembrane helices of GlyT1^{minimal}, and screened the constructs on the basis of their expression level, thermal stability and ability to bind inhibitor. In total, we introduced 329 single mutations into the minimal construct, of which we combined the point mutations L153A, S297A, I368A and C633A in the final construct for crystallization. In addition, we omitted the N-terminal residue 91 from the GlyT1–Lic sequence, and residues 9–281 of lichenase (PDB ID 2CIT) have been fused at the N terminus in order to increase the hydrophilic surface area of the transporter and to facilitate crystallization. The sequences of GlyT1 and GlyT1–Lic followed by a C-terminal enhanced green fluorescent protein (eGFP) and a decahistidine tag were cloned into a pCDNA3.1 vector for transient transfection in human embryonic kidney (HEK293) cells (Invitrogen; not authenticated and not tested for mycoplasma contamination), and a pFastBac vector for baculovirus expression in *Spodoptera frugiperda* (*Sf9*) insect cells (American Type Culture Collection (ATCC), catalogue number CRL-1711; authenticated and free of mycoplasma contamination), respectively.

Transporter expression and purification

GlyT1 was expressed in FreeStyle 293 expression medium (Thermo Fisher Scientific) in 1-litre scale in 600 ml TubeSpin bioreactors, incubating in an orbital shaker at 37 °C, 8% CO_2 and 220 rpm in a humidified atmosphere. The cells were transfected at a density of 1×10^6 cells per ml and a viability of above 95%. A 25 kDa linear polyethylenimine (LPEI) was used as the transfection reagent, at a GlyT1 DNA:LPEI ratio of 1:2. The cells were typically collected 60 h post-transfection at a viability of around 70%, and stored at −80 °C until purification.

GlyT1–Lic was expressed in 20–25-litre scale in 50-litre single-use WAVE bioreactors (CultiBag RM, Sartorius Stedim Biotech) at 27 °C with 18–25 rocks per minute in a 40% oxygenated Sf900-III medium (Gibco by Life Technologies). The cells were typically infected with a 0.25% volume of infection of the virus at a density of $2–3 \times 10^6$ cells per ml and viability of above 95%. The cells were collected 72 h post-infection at a viability of around 80%, and stored at −80 °C until purification.

Purification of GlyT1 constructs has been described previously[28]. In brief, the biomass was solubilized in 50 mM Tris-HCl pH 7.5, 150 mM NaCl, 100 μM Cmpd1 ([5-methanesulfonyl-2-(2,2,3,3,3-pentafluoro-propoxy)-phenyl]-[5-tetrahydro-pyran-4-yloxy)-1,3-dihydro-isoindol-2-yl]-methanone) and 15–25 μM brain polar lipids extract (Avanti), containing either 1% (w/v) lauryl maltose neopentyl glycol (LMNG) or 1% (w/v) decyl maltose neopentyl glycol (DMNG) and 0.1% cholesteryl hemisuccinate (CHS). The protein was purified by batch purification using TALON affinity resin (GE Healthcare), then treated with HRV-3C protease (Novagen) to cleave the eGFP–His tag and Roche PNGase F (from *Flavobacterium meningosepticum*) to trim glycosylation (Supplementary Fig. 2). The transporter was concentrated typically to 15–30 mg ml^{-1} in the final buffer, containing 50 mM Tris-HCl pH 7.5, 150 mM NaCl, 50 μM inhibitor and 15–25 μM brain polar lipids extract, and 0.01% LMNG (w/v) plus 0.001% CHS for GlyT1, and either 0.05% (w/v) LMNG plus 0.005% CHS or 0.01% DMNG plus 0.001% CHS for the GlyT1–Lic construct.

Lipidic cubic phase crystallization

Before crystallization, the concentrated GlyT1 was incubated with Sb_GlyT1#7 in a 1:1.2 molar ratio (GlyT1:sybody) and 1 mM inhibitor. The protein solution was reconstituted into mesophase using molten monoolein (Molecular Dimensions) spiked with 5% (w/w) cholesterol (Sigma) at a 2:3 ratio of protein solution:lipid, using two coupled Hamilton syringes. Crystallization trials were carried out in 96-well glass sandwich plates (VWR) by a Gryphon LCP crystallization robot or a Mosquito LCP dispensing robot in a humidified chamber, using 50–100 nl of mesophase overlaid with 800 nl of crystallization solution. The plates were incubated at 19.6 °C and inspected manually. Crystals appeared within 3–10 days in 0.1 M ADA pH 7, 13–25% PEG600 and 4–14% v/v (±)-1,3-butanediol, with the longest crystal dimension being 2–5 μm. For crystallization of GlyT1 with Sb_GlyT1#7, we also used 3% v/v dimethyl sulfoxide, 3% v/v glycerol, 0.2 M NDSB-201, 0.2 M NDSB-211, 0.2 M NDSB-221, 0.05% w/v 1,2,3-heptanetriol or 4% v/v 1,3-propanediol (Hampton research) as additives. The micrometre-sized crystals werecollected from the LCP matrix using MiTeGen MicroMounts, and flash frozen in liquid nitrogen.

Data collection and structure determination

Crystallographic data were collected on the P14 beamline operated by EMBL Hamburg at the PETRA III storage ring (DESY, Hamburg), using the 5×10 μm^2 (vertical × horizontal) microfocus beam, with a total photon flux of 1.3×10^{13} photons per second at the sample position. Diffraction data were recorded on an EIGER 16M detector. In our data-collection strategy, we typically defined a region of interest of 60×14 μm^2 to 290×340 μm^2 on the loop, containing crystals oriented perpendicularly to the incoming beam. Diffraction data were collected using serial helical line scans[41], with a sample displacement of 1 μm along the rotation axis during the acquisition of one frame, an oscillation of 0.2°, and an exposure time of 0.1 s, with 100% transmission.

Dozor[42,43] was used for the first step of data processing to identify diffraction patterns within the large set of frames. Each diffraction image was analysed by Dozor, which determined a list of coordinates for diffraction spots and their partial intensities, and generated a diffraction heat map.

Diffraction data were indexed and integrated using XDS[44,45], and the resulting partial mini datasets, containing 3–20 consecutive images, were scaled with XSCALE[45]. In some cases, mini datasets with adjacent frame numbers were merged into longer datasets (more than 20 frames) manually. One rotation dataset of 20 frames with an oscillation of 1.0° is included in the GlyT1–Lic dataset.

Our choice of partial mini datasets to be merged into a high-quality complete dataset was guided by an inhouse script, Ctrl-d, which measured the correlation of each mini dataset to the rest of the mini datasets. The important criterion was the requirement for enough collected datasets to have a scaling model for robust estimation of outliers.

We carried out a total of 514 two-dimensional (2D) helical scans on 409 mounted loops containing microcrystals of GlyT1, resulting in the collection of 1,365,232 diffraction patterns, of which 30,837 frames contained more than 15 diffraction spots. We indexed and integrated 229 mini datasets, of which 207, containing 3,400 frames, with a correlation of above 0.7 were scaled and merged (Extended Data Figs. 9a, c). For GlyT1–Lic, a total of 1,733 2D helical scans were performed on 1,222 mounted loops containing microcrystals, resulting in the collection of 3,190,397 diffraction images of which 225,037 contained 15 spots or more. We indexed and integrated 249 mini datasets, of which 213, containing 3,906 diffraction patterns, with a correlation of above 0.5 were scaled and merged (Extended Data Fig. 9b, d).

The structure of the GlyT1–sybody complex was solved by molecular replacement using modified models of MhsT (PDB ID 4US3) and SERT (PDB ID 6DZZ) (with the loops, TM12 and C-terminal tail removed from the original models), as well as an ASC-binding nanobody (PDB ID 5H8D), as separate search models in Phaser. To solve the structure

of GlyT1–Lic, we used the lichenase fusion protein structure (PDB ID 2CIT) as the third search model. The models were refined with Buster, followed by visual examination and manual rebuilding in Coot and ISOLDE[46–48]. The final model of GlyT1 lacks the first 8 residues of the N terminus, residues 235–237 in EL2, residues 309–314 in TM5 and the last 20 residues of the C terminus. Of two lichenase fusion proteins in the asymmetric unit of the GlyT1–Lic structure, only one chain (with higher B factors compared with the other protein chains) has been modelled, owing to the high flexibility of the chains and poor density of the region. The final model of GlyT1–Lic further lacks the first 13 residues of N terminus, residues 235–239 in EL2, residues 309–315 in TM5 and the last 34 residues of the C terminus in chain A; and the first 15 residues of the N terminus, residues 235–239 in EL2, residues 309–315 in TM5 and the last 20 residues of the C terminus in chain B. Of the GlyT1 and GlyT1–Lic residues, 95.4% and 95.01%, respectively, are within the Ramachandran favoured region, with 0.15% (one residue) and 0.26% (four residues) being outliers. The final data and refinement statistics are presented in Extended Data Table 1. Statistics on data collection were calculated using phenix.table_one[49].

Scintillation proximity assays

Scintillation proximity assays (SPAs) were carried out in 96-well plates (Optiplate, Perkin Elmer) using copper His-tag YSi SPA beads (Perkin Elmer) and [^{3}H]Org24598 (80 Ci mmol^{-1}). Reactions took place in assay buffer containing 50 mM Tris-HCl pH 7.5, 150 mM NaCl and 0.001% LMNG supplemented with solubilized GlyT1 cell membrane/SPA mix (0.3 mg per well) and for competition experiments, a tenfold serial dilution series of nonlabelled inhibitor Cmpd1 (final concentration 0.001 nM to 10 μM), bitopertin (0.001 nM to 10 μM), or glycine (0.1 nM to 1 mM). Assays were incubated for 1 h at 4 °C before values were read out using a top count scintillation counter at room temperature. In thermal shift (TS) scintillation proximity assays (SPA–TS), solubilized protein was incubated for 10 min with a temperature gradient of 23–53 °C across the wells in a Techne Prime Elite thermocycler before mixing with SPA beads.

FSEC–TS

A fluorescence-detection size-exclusion chromatography thermostability (FSEC–TS) assay was used to evaluate the thermostability of constructs[50]. We dispensed 180-μl aliquots of solubilized GlyT1-containing cell membrane in a 4 °C cooled 96-well polymerase chain reaction (PCR) plate (Eppendorf) in triplicates. A gradient of 30–54 °C for 10 min was applied on the plate in a BioRad Dyad thermal cycler. The plate was cooled on ice and 40 μl of the samples were injected into a 300-mm Sepax column in 50 mM Tris-HCl pH 7.5, 150 mM NaCl and 0.001% LMNG; the SEC profile was monitored using the fluorescence signal from the eGFP tag.

Thermofluor stability assay

For Thermofluor stability assays, we used a GlyT1^{minimal} construct (containing N- and C-terminal deletions of residues 1–90 and 685–706, respectively), expressed in *Sf*9 insect cells and purified as above. Purified GlyT1^{minimal} was diluted in 50 mM Tris-HCl pH 7.5, 150 mM NaCl and 0.001% LMNG to a final concentration of 0.73 μM and distributed into the wells of a 96-well PCR plate on ice. The inhibitor was added to the wells at a final concentration of 10 μM, and a corresponding amount of dimethylsulfoxide (DMSO) was added to the control wells. The plate was sealed and incubated for 30 min on ice. A 1:40 (v/v) working solution of the CPM (*N*-[4-(7-diethylamino-4-methyl-3-coumarinyl) phenyl]maleimide) dye stock (4 mg ml^{-1} in DMSO) was prepared; 10 μl of this solution was added to 75 μl of protein sample in each well and mixed thoroughly. We adapted a published assay[51] based on CPM dye to perform the stability tests. The melting profiles were recorded using a real-time PCR machine (Rotor-Gene Q, Qiagen) with temperature ramping from 15 °C to 95 °C at a heating rate of 0.2 °C s^{-1}. The melting temperatures (T_m) were calculated from the point of inflection, based on a fit to the Boltzmann equation.

Molecular modelling

We used the 3D conformer generator Omega (OpenEye) to generate a conformational ensemble for bitopertin. Each conformer was superimposed via ROCS (OpenEye)[52] onto the transporter-bound conformation of Cmpd1, and the overlay was optimized with respect to similarity of 3D shapes. The highest-scoring conformer was retained and energy-minimized within the binding pocket using MOE[53]. Docking was performed using the software GOLD[54] from the Cambridge Crystallographic Data Centre (CCDC) with default settings and the standard scoring function ChemPLP. An additional energy minimization within the binding pocket was performed using the five best docking poses.

Rapido was used for structure superpositions[55]. A total number of 513, 414 and 393 residues were used to align the structures of SERT (PDB ID 6DZZ), LeuT (PDB ID 3TT3) and MhsT (PDB ID 4US3) on that of GlyT1. Residue ranges used for alignment were 104–224, 226–232, 259–306, 316–353, 357–388, 390–433, 438–489, 491–632 and 636–652 of GlyT1 and 83–152, 154–204, 206–212, 222–239, 242–271, 281–318, 322–353, 355–398, 404–597 and 600–616 of SERT in the SERT–GlyT1 superposition; 115, 117–211, 215–219, 262–270, 272–278, 281, 288–307, 317–352, 354–374, 376–387, 390–421, 429–489, 496–519, 522–530, 532–559 and 568–592 of GlyT1 and 21–68, 71–73, 76–80, 82–87, 90–123, 126–130, 141–156, 160, 166–185, 196–217, 222–240, 242–257, 259–270, 273–291, 293–305, 307–312, 318–372, 374–406, 408–435 and 444–468 of LeuT in the GlyT1–LeuT superposition; and 119–173, 176–210, 264–271, 318–352, 358–422, 432–487, 532–554, 568–595, 493–517 and 287–306 of GlyT1 and corresponding residues 28–82, 88–122, 134–141, 178–212, 218–282, 284–339, 389–411, 421–448, 343–367 and 148–167 of MhsT in the GlyT1–MhsT superposition.

[^{3}H]Glycine-uptake assay

We carried out glycine-uptake assays for the wild-type and crystallization constructs of GlyT1 and for untransfected cells in $n = 5$, $n = 4$ and $n = 3$ independent experiments, respectively, each performed with 6–11 replicate measurements of total and nonspecific uptake. Mammalian HEK293-MSR cells (Invitrogen; not authenticated and not tested for mycoplasma contamination) were plated at a density of 40% in 96-well plates and were transfected with 0.1 μg of DNA (in pXOON plasmids) per well in complex with Ecotransfect transfection reagent (OZ Bioscience), along with untransfected cells, 48 h before uptake assays. The medium was aspirated after 48 h and the cells were washed with uptake buffer containing 10 mM HEPES-Tris pH 7.4, 150 mM NaCl, 1 mM $MgSO_4$, 5 mM KCl and 10 mM (+)D-glucose. The cells were incubated for 30 min at 22 °C with the uptake buffer containing no inhibitor (total uptake) or 10 μM Cmpd1 (nonspecific uptake). Glycine uptake was initiated by adding either [^{3}H]glycine (15 Ci mmol^{-1}) to a final concentration of 1 μM for total uptake or [^{3}H]glycine (15 Ci mmol^{-1}) and Cmpd1 to a final concentration of 1 μM and 10 μM, respectively, for nonspecific uptake. The plates were incubated for 10 min or for variable time points and radiotracer-uptake reactions were stopped by aspiration of the substrate followed by washing with 200 μl of the uptake buffer in an automated plate washer. The cells were then lysed with Microscint 20 (Perkin Elmer) and shaken for 1 h; radioactivity was measured by a Topcounter NXT (Packard). Specific uptake was determined by subtracting nonspecific uptake from total uptake. Statistical significance was determined using one sample *t*-tests with alpha = 0.05.

[^{3}H]Glycine-uptake-inhibition assay

Glycine-uptake-inhibition assays were performed in quadruplicate and according to a method previously described[24]. In brief, mammalian Flp-in-CHO cells (Invitrogen; authenticated and free of mycoplasma contamination) were transfected with human and mouse GlyT1 and human GlyT2 cDNA and were plated at a density of 40,000 cells per well in complete F-12 medium 24 h before uptake assays. The medium was aspirated the next day and the cells were washed twice with uptake buffer containing 10 mM HEPES-Tris pH 7.4, 150 mM NaCl, 1 mM $CaCl_2$,

2.5 mM KCl, 2.5 mM $MgSO_4$ and 10 mM (+)D-glucose. The cells were incubated for 20 min at 22 °C with no inhibitor, 10 mM nonradioactive glycine, or a concentration range of the inhibitor to calculate IC_{50} value. A solution containing 25 µM nonradioactive glycine and 60 nM [^{3}H] glycine (11–16 Ci mmol^{-1}) (hGlyT1 and mGlyT1) or 200 nM [^{3}H]glycine (hGlyT2) was then added. Nonspecific uptake was determined with 10 µM Org24598 (a hGlyT1 and mGlyT1 inhibitor)[27], or 5 µM Org25543 (a hGlyT2 inhibitor)[56]. The plates were incubated for 15 min (hGlyT1) or 30 min (mGlyT1 and hGlyT2) with gentle shaking, and reactions were stopped by aspiration of the mixture and washing three times with ice-cold uptake buffer. The cells were lysed and shaken for 3 h; radioactivity was measured by a scintillation counter. The assays were performed in quadruplicate.

To evaluate the mode of inhibition of Cmpd1, we carried out glycine-uptake assays for wild-type GlyT1 as described in the section '[^{3}H] Glycine-uptake assay' above. The assays were performed in four independent experiments, each with two replicate measurements for total uptake and one replicate measurement for nonspecific uptake. Experiments to generate all four $K_m - V_{max}$ curves for the inhibitor were performed simultaneously on the same 96-well plate. Glycine uptake was initiated by adding the specified concentrations of [^{3}H]glycine (15 Ci mmol^{-1}) mixed with unlabelled glycine in a 1:1,000 ratio (10 µM, 25 µM, 50 µM, 100 µM, 200 µM, 350 µM, 500 µM and 700 µM) and mixed with 0 nM, 60 nM, 240 nM and 960 nM of Cmpd1. The plate was incubated for 10 min, and radiotracer-uptake reactions were stopped by aspiration of the substrate followed by washing with 200 µl of the uptake buffer in an automated plate washer. The cells were then lysed with Microscint 20 (Perkin Elmer) and shaken for 1 h; radioactivity was measured by a Topcounter NXT (Packard). Specific uptake was determined by subtracting nonspecific uptake from total uptake. Statistical significance was determined using one sample *t*-tests with alpha = 0.05. Data were fitted to Michaelis–Menten kinetics using nonlinear regression and transformed to Eadie–Hofstee plots with subsequent linear regression analysis using GraphPad Prism 9.

[^{3}H]Org24598-binding assay

[^{3}H]Org24598-binding experiments were performed in quadruplicate as described[24]. Membranes from Chinese hamster ovary (CHO) cells expressing hGlyT1 and membranes extracted from mouse forebrains (expressing mGlyT1) were used for binding assays. Saturation isotherms were determined by adding [^{3}H]Org24598 to mouse forebrain membranes (40 µg per well) and cell membranes (10 µg per well) in a total volume of 500 µl for 3 h at room temperature. Membranes were incubated with 3 nM [^{3}H]Org24598 and ten concentrations of Cmpd1 for 1 h at room temperature. Reactions were terminated by filtering the mixture onto a Unifilter with bonded GF/C filters (PerkinElmer) presoaked in binding buffer containing 50 mM sodium-citrate pH 6.1, for 1 h and washed three times with 1 ml of the same cold binding buffer. Filtered radioactivity was counted on a scintillation counter. Nonspecific binding was measured in the presence of 10 µM Org24598.

Figure preparation

Figures showing protein structures were prepared using the PyMOL 2.3.3 Incentive Product from Schrodinger, LLC. Sequences were aligned using ClustalOmega[57] and the relevant figure prepared using BOXSHADE 3.2. Binding and uptake data were analysed and figures prepared using GraphPad Prism 9.

Reporting summary

Further information on research design is available in the Nature Research Reporting Summary linked to this paper.

Data availability

Coordinates and structure factors for the structures of GlyT1 at 3.4 Å and 3.9 Å resolution have been deposited in the Protein Data Bank (https://www.rcsb.org) under accession codes 6ZBV and 6ZPL, respectively. The executable Ctrl-d is available via webapps.embl-hamburg.de.

42. Zander, U. et al. MeshAndCollect: an automated multi-crystal data-collection workflow for synchrotron macromolecular crystallography beamlines. *Acta Crystallogr. D* **71**, 2328–2343 (2015).
43. Popov, A. N. & Bourenkov, G. *Dozor* (European Synchrotron Radiation Facility, 2016).
44. Tange, O. GNU Parallel: the command-line power tool. *The USENIX Magazine* **36**, 42–47 (2011).
45. Kabsch, W. XDS. *Acta Crystallogr. D* **66**, 125–132 (2010).
46. Emsley, P., Lohkamp, B., Scott, W. G. & Cowtan, K. Features and development of Coot. *Acta Crystallogr. D* **66**, 486–501 (2010).
47. Bricogne, G. et al. *BUSTER* v.2.10.3 (Global Phasing, 2019).
48. Croll, T. I. ISOLDE: a physically realistic environment for model building into low-resolution electron-density maps. *Acta Crystallogr. D* **74**, 519–530 (2018).
49. Liebschner, D. et al. Macromolecular structure determination using X-rays, neutrons and electrons: recent developments in Phenix. *Acta Crystallogr. D* **75**, 861–877 (2019).
50. Hattori, M., Hibbs, R. E. & Gouaux, E. A fluorescence-detection size-exclusion chromatography-based thermostability assay for membrane protein precrystallization screening. *Structure* **20**, 1293–1299 (2012).
51. Alexandrov, A. I., Mileni, M., Chien, E. Y. T., Hanson, M. A. & Stevens, R. C. Microscale fluorescent thermal stability assay for membrane proteins. *Structure* **16**, 351–359 (2008).
52. Hawkins, P. C. D., Skillman, A. G. & Nicholls, A. Comparison of shape-matching and docking as virtual screening tools. *J. Med. Chem.* **50**, 74–82 (2007).
53. Molecular Operating Environment (MOE) 2019.01 (Chemical Computing Group, 2019).
54. Jones, G., Willett, P., Glen, R. C., Leach, A. R. & Taylor, R. Development and validation of a genetic algorithm for flexible docking. *J. Mol. Biol.* **267**, 727–748 (1997).
55. Mosca, R. & Schneider, T. R. RAPIDO: a web server for the alignment of protein structures in the presence of conformational changes. *Nucleic Acids Res.* **36**, W42–W46 (2008).
56. Caulfield, W. L. et al. The first potent and selective inhibitors of the glycine transporter type 2. *J. Med. Chem.* **44**, 2679–2682 (2001).
57. Madeira, F. et al. The EMBL-EBI search and sequence analysis tools APIs in 2019. *Nucleic Acids Res.* **47** (W1), W636–W641 (2019).
58. Ashkenazy, H. et al. ConSurf 2016: an improved methodology to estimate and visualize evolutionary conservation in macromolecules. *Nucleic Acids Res.* **44** (W1), W344–W350 (2016).
59. Winn, M. D. et al. Overview of the CCP4 suite and current developments. *Acta Crystallogr. D* **67**, 235–242 (2011).
60. Kantcheva, A. K. et al. Chloride binding site of neurotransmitter sodium symporters. *Proc. Natl Acad. Sci. USA* **110**, 8489–8494 (2013).
61. Zhang, Y.-W. et al. Chloride-dependent conformational changes in the GlyT1 glycine transporter. *Proc. Natl Acad. Sci. USA* (in the press) (2021).
62. Singh, S. K., Piscitelli, C. L., Yamashita, A. & Gouaux, E. A competitive inhibitor traps LeuT in an open-to-out conformation. *Science* **322**, 1655–1661 (2008).
63. Diederichs, K., & Karplus, P. A. Improved R-factors for diffraction data analysis in macromolecular crystallography. *Nat. Struct. Mol. Biol.* **4**, 269–275 (1997).
64. Diederichs, K., & Karplus, P. A. Linking crystallographic model and data quality. *Science.* **336**, 1030–1033 (2012).

Acknowledgements We thank R. Thoma (F. Hoffmann-La Roche) for long-term project support and discussions; L. Hetemann and J. Gera for early contributions to producing the mutants; J. Thornton for advice and discussions on the project; F. Dall'Antonia for writing the Ctrl-d script; J. Pieprzyk for assistance with mammalian cell expression; H. Poulsen for assistance with electrophysiology studies; M. M. Garcia Alai for access to sample preparation and crystallization facilities at EMBL Hamburg; and I. M. Nemtanu and C. Guenther for technical assistance. We acknowledge the support offered at the P14 beamline operated by EMBL Hamburg at the PETRA III storage ring (DESY, Hamburg). We thank J. A. Lyons, B. Pedersen, C. Löw and the PROMEMO Center of Excellence of the Danish Research Foundation for discussions. This project has received funding from Novo Nordisk Foundation (to P.N.), the Lundbeck Foundation via the DANDRITE Neuroscience Center, and F. Hoffmann-La Roche. A.S. was supported by a fellowship from the EMBL Interdisciplinary Postdoc (EIPOD) programme under Marie Sklodowska-Curie Actions COFUND (grant agreement number 664726).

Author contributions R.J.P.D. initiated and designed the project with P.N. and T.R.S. at Roche, Aarhus University and EMBL. Construct design was by R.J.P.D. and construct screening was by P.S., A.S. and R.J.P.D. Expression was carried out by P.S., M.S. and A.S. Purification was carried out by P.S. and A.S. Radioligand, thermal-shift and uptake assays were performed by E.P., P.S. and S.S. Sybody was generated by I.Z., M.A.S., P.S. and R.J.P.D. Crystallization, data collection and processing, and structure refinement were carried out by A.S. Serial data collection was established by A.S., G.B. and T.R.S. Dozor and serial data processing scripts were modified by G.B. Molecular modelling and docking were done by W.G. The manuscript was written by A.S., R.J.P.D. and P.N. with contributions from T.R.S., G.B., W.G. and S.S.

Competing interests P.S., M.S., W.G. and E.P. are employees of F. Hoffmann-La Roche. I.Z., R.J.P.D. and M.A.S. are co-founders and shareholders of Linkster Therapeutics AG.

Additional information
Supplementary information The online version contains supplementary material available at https://doi.org/10.1038/s41586-021-03274-z.
Correspondence and requests for materials should be addressed to T.R.S., R.J.P.D. or P.N.
Peer review information *Nature* thanks Carmen Villmann and the other, anonymous, reviewer(s) for their contribution to the peer review of this work. Peer reviewer reports are available.

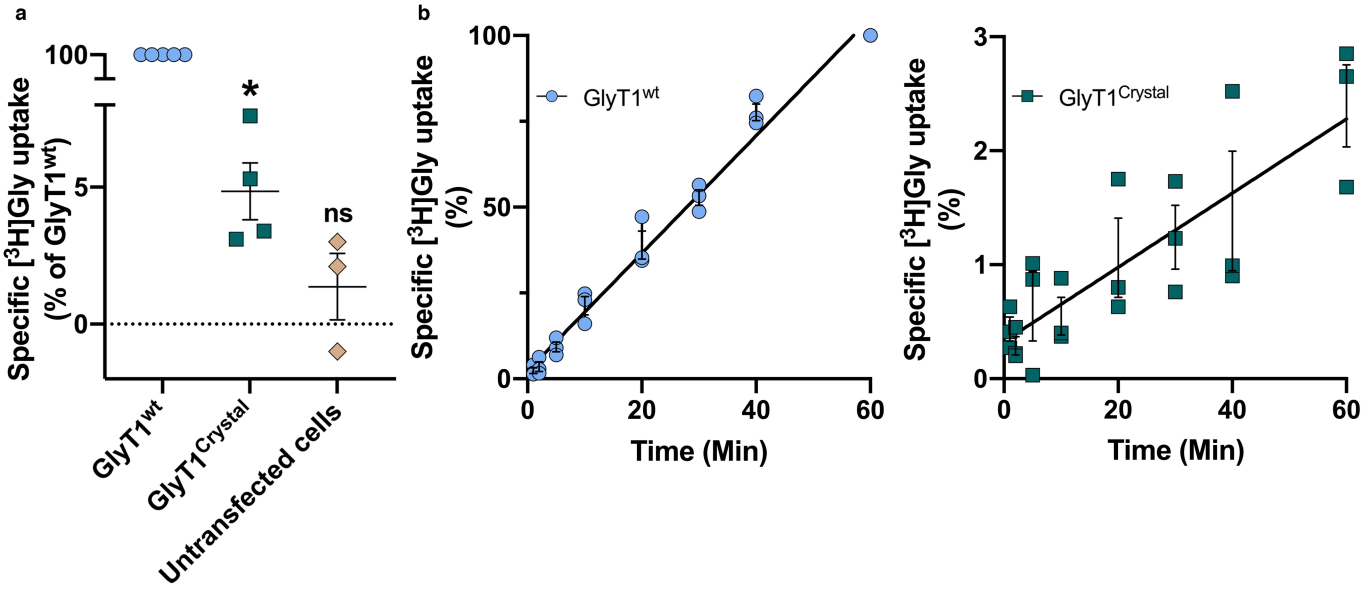

Extended Data Fig. 1 | GlyT1 activity. a, Specific [^{3}H]glycine uptake, after 10 min of incubation, by cells transfected with the crystallization construct of GlyT1 (GlyT1^{Crystal}) and by untransfected cells, normalized to uptake by wild-type GlyT1 (GlyT1^{wt}). Specific uptake was determined by subtracting nonspecific uptake (with 1 µM [^{3}H]glycine plus 10 µM Cmpd1) from total uptake (with 1 µM [^{3}H] glycine only) and was subjected to one-sample *t*-tests (two-tailed, not corrected for multiple corrections). Specific uptake by GlyT1^{Crystal} was significantly different from zero ($P = 0.0185$); untransfected cells, by contrast, showed no statistically significant specific glycine-transport capacity ($P = 0.3764$). Data points are averages from $n = 5$, $n = 4$ and $n = 3$ independent experiments for GlyT1^{wt}, GlyT1^{Crystal} and untransfected cells, respectively, each performed with 6–11 measurements. Error bars represent standard error of the mean (****$P < 0.0001$; **$P < 0.01$; *$P < 0.05$). **b**, Time-course experiments performed as in **a** with variable incubation times, showing that uptake increases linearly within the first 60 min for both GlyT1^{wt} and GlyT1^{Crystal}, consistent with the occurrence of active transport. Data were subjected to linear regression analysis, yielding $r^2 = 0.99$ and $r^2 = 0.97$ for GlyT1^{wt} and GlyT1^{Crystal}, respectively. Shown are means ± s.e.m. of normalized data points from $n = 3$ independent experiments, each performed in duplicate. Error bars represent s.e.m.

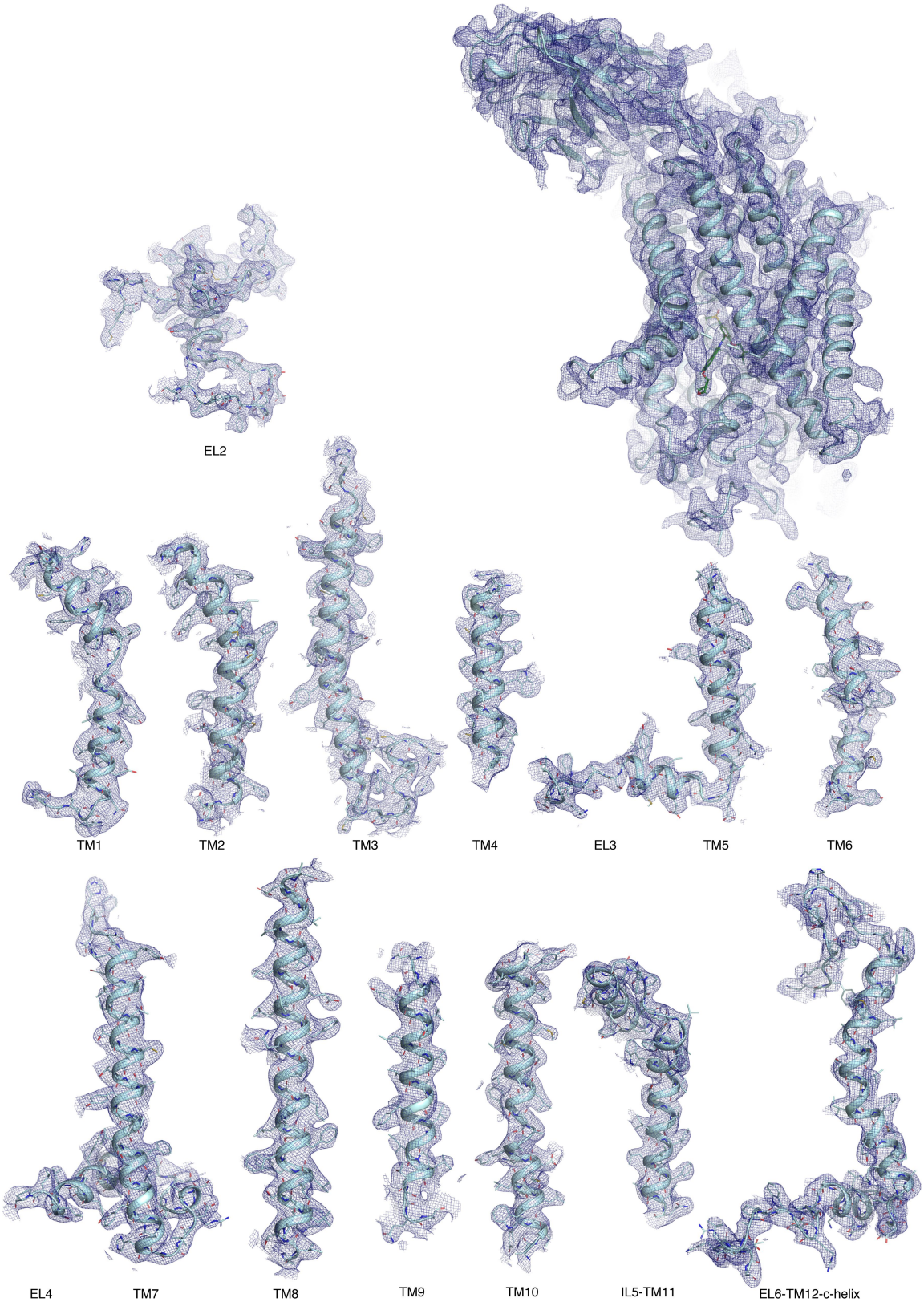

Extended Data Fig. 2 | Atomic model and electron density map of the human GlyT1–sybody complex with bound Cmpd1. The overall structure of the GlyT1–sybody complex (cyan) with bound Cmpd1 (green) (top right) and magnified views of separate transmembrane helices, intracellular loops and extracellular loops (below and to the left) are shown in $2F_o - F_c$ electron density maps (blue) countered at 1.0 r.m.s.d.

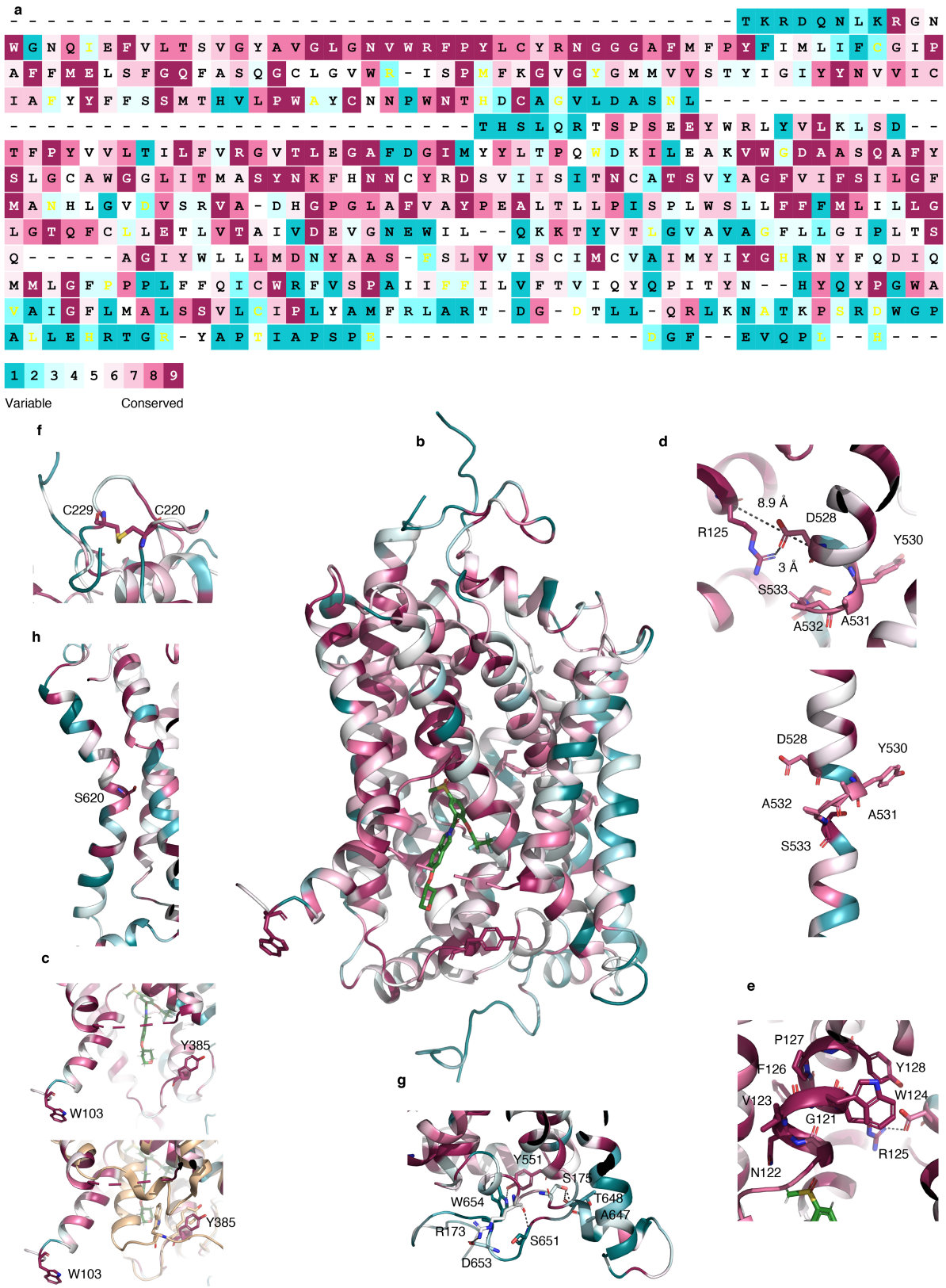

Extended Data Fig. 3 | Sequence conservation of hGlyT1. a, **b**, Sequence (**a**) and overall structure (**b**) of human GlyT1, coloured on the basis of ConSurf[58]. **c**, Top, disrupted interaction between conserved residues W103 (in TM1a) and Y385 (in TM6) owing to the hinge-like motion of TM1a in the inward-open structure of hGlyT1 bound to Cmpd1; bottom, overlay of inward-facing occluded MhsT (wheat) on inward-open GlyT1. **d**, Top, the closed extracellular gate between D528 (TM10) and R125 (TM1). Bottom, a short nonhelical region is observed in TM10 at the partially conserved Y530AAS533 sequence that supposedly allows a local flexibility for opening and closing of the extracellular gate between TM10 and TM1. **e**, The close packing of the extracellular vestibule around W124 in the conserved GNVWRFPY motif. **f**, The strictly conserved disulfide bridge (C220–C229) on EL2. **g**, The C-terminal tail of the transporter forms a cap over the intracellular face, stabilized by interactions with IL1 and IL5. The interacting residues are shown. **h**, Similar to dDAT and hSERT, TM12 of GlyT1 kinks at S620 of the G613(X_6)S(X_4)P625 motif conserved in eukaryotic NSS transporter. Residue S620 at the kink of TM12 is shown.

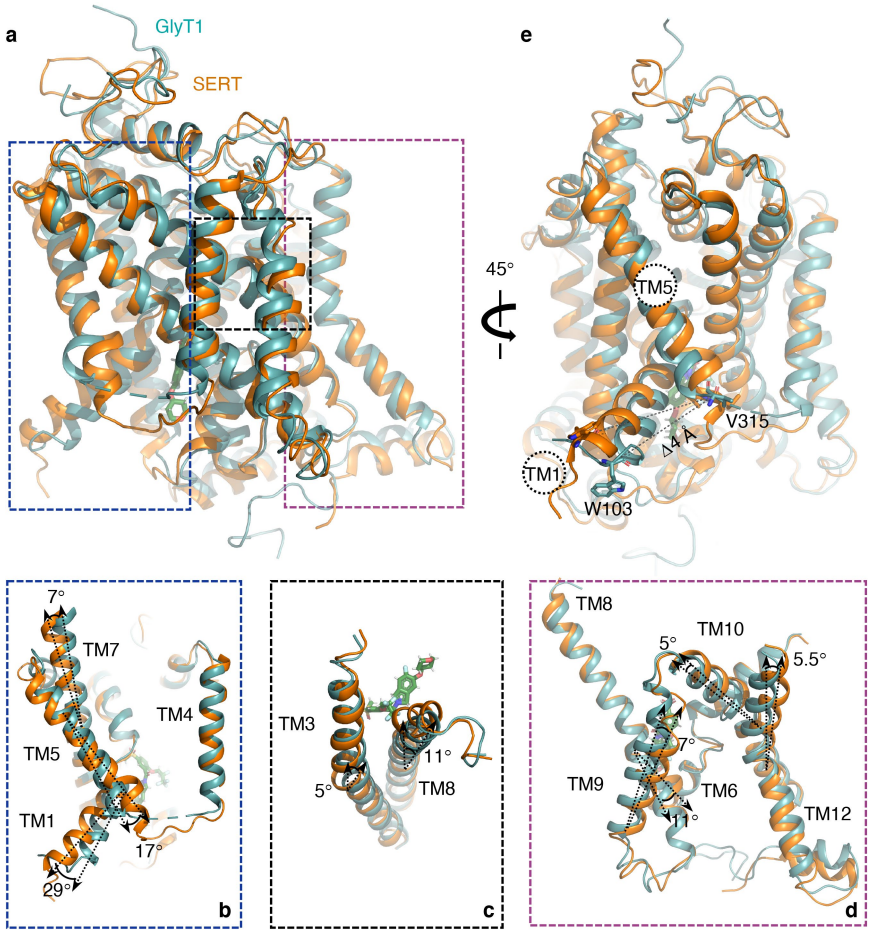

Extended Data Fig. 4 | Comparison of the inward-open structures of GlyT1 and SERT. a, Superposition of the secondary structures of GlyT1 (cyan) and SERT (orange) using the so-called scaffold helices TM3–TM4 and TM8–TM9. The TM regions with structural differences are boxed, with magnified views shown in **b**–**d**. **b**, The intracellular half of TM1 and extracellular half of TM7 are, by 29° and 7°, respectively, closer to the core in GlyT1 compared with the corresponding TMs in inward-open SERT, and the intracellular half of TM5 has splayed 17° further from the core. **c**, Halfway across the membrane, TM3 in GlyT1 is locally 5° closer to the core than in SERT. The intracellular half of TM8 has splayed by 11° further away from the core of GlyT1 compared with SERT. **d**, On the extracellular side, TM9 is by 7° moved away from TM12, TM10 has shifted by 5° away from TM6 and TM12 is tilted by 5.5° towards the core of GlyT1. The 11° difference at the intracellular half of TM8 is also depicted. **e**, The intracellular gate to the core of GlyT1 defined by TM1a and TM5 is by 4 Å more closed than that of inward-open structure of SERT. Cα atoms of the conserved residues W103 of TM1a and V315 of TM5 were used for the measurements.

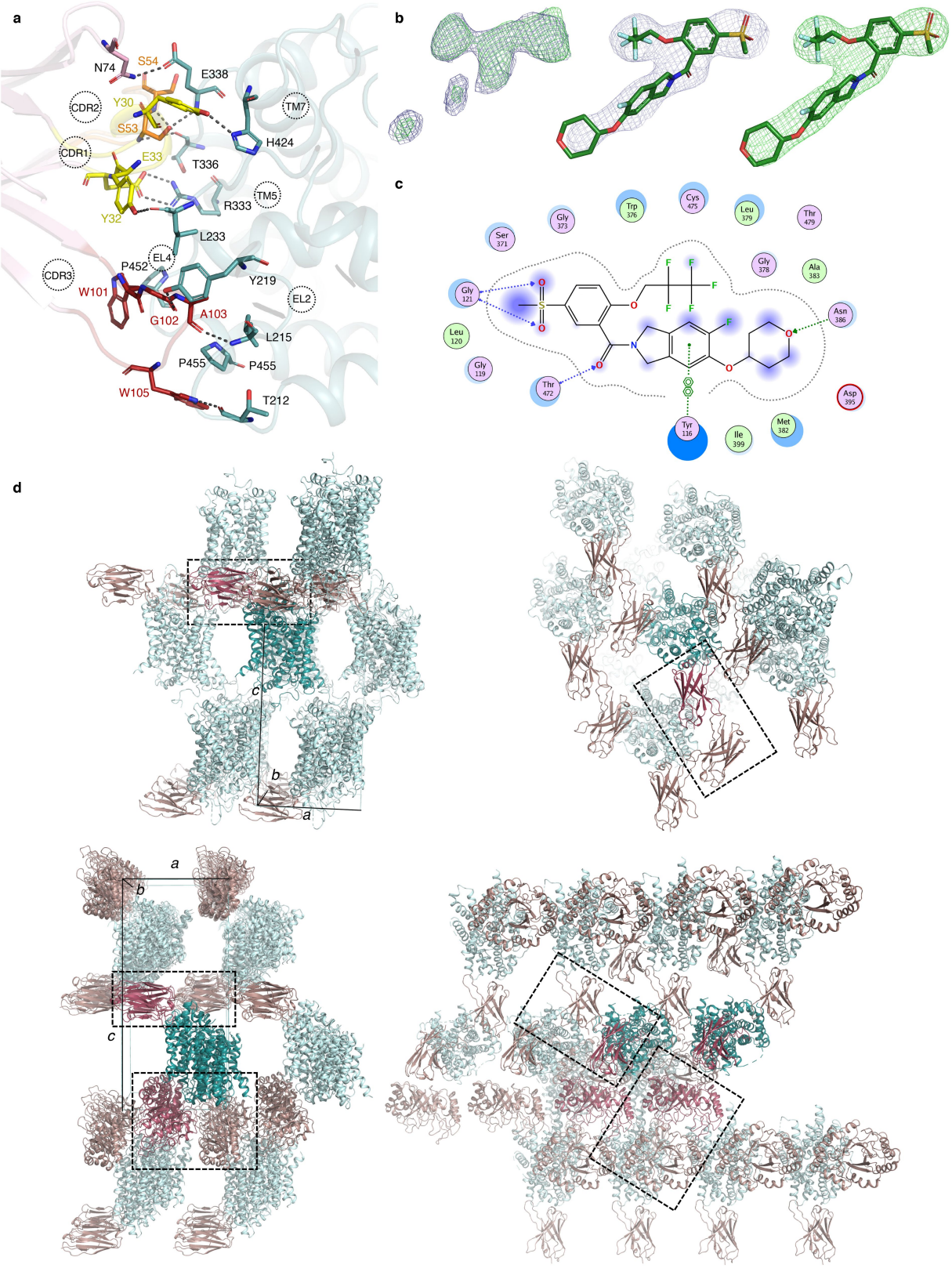

Extended Data Fig. 5 | See next page for caption.

Extended Data Fig. 5 | Detailed view of the GlyT1–sybody interface and protein–inhibitor interactions, electron density maps of Cmpd1, and crystal packing of GlyT1 and GlyT1–Lic. a, Sybody Sb_GlyT1#7 binds to the extracellular segment of GlyT1 through several interactions between the long complementarity-determining region 3 (CDR3), CDR2 and CDR1 of Sb_GlyT1#7 and EL2, EL4, TM5 and TM7 of the transporter. The interface of GlyT1 and sybody was analysed using contact as a part of the CCP4 program suit[59]. Interacting residues of CDR1 (yellow), CDR2 (orange) and CDR3 (red) of the sybody and EL2, EL4 and the extracellular ends of TM5 and TM7 of GlyT1 (cyan) are depicted. **b**, Left, unbiased $F_o - F_c$ (green) and $2F_o - F_c$ (blue) electron density maps of Cmpd1 before placement of the inhibitor, contoured at 3.0 r.m.s.d. and 0.8 r.m.s.d., respectively. Centre, $2F_o - F_c$ (blue) electron density map contoured at 1.0 r.m.s.d. after placement of the inhibitor and refinement. No residual $F_o - F_c$ density is observed above 2.0 r.m.s.d. after refinement. Right, $F_o - F_c$ simulated annealing composite omit map[49] of Cmpd1 (a prominent 11.0 r.m.s.d. signal in an unbiased difference map) at 8.2 r.m.s.d. **c**, Diagram showing protein–ligand interactions calculated with MOE. Several hydrogen bonds that contribute to ligand binding are shown with dotted arrows (with backbone interactions in blue and side-chain interactions in green). The π-stacking interaction between the isoindoline scaffold of the ligand and Y116 is shown. Hydrophilic residues are in purple; blue rings indicate basic groups; red rings indicate acidic groups; and hydrophobic residues are in green. **d**, Crystal lattice arrangements viewed from the side and top of GlyT1 (top) and of GlyT1–Lic (bottom). In GlyT1, crystal contacts exist between adjacent sybodies. In GlyT1–Lic, sybodies form the crystal contacts on the extracellular side and adjacent lichenase fusion proteins do so on the intracellular side. Dashed boxes show the locations of crystal contacts. Unit cell dimensions *a*, *b*, *c* in GlyT1 and GlyT1–Lic are 65.17 Å, 58.14 Å, 122.31 Å and 116.41 Å, 69.71 Å, 149.43 Å, respectively.

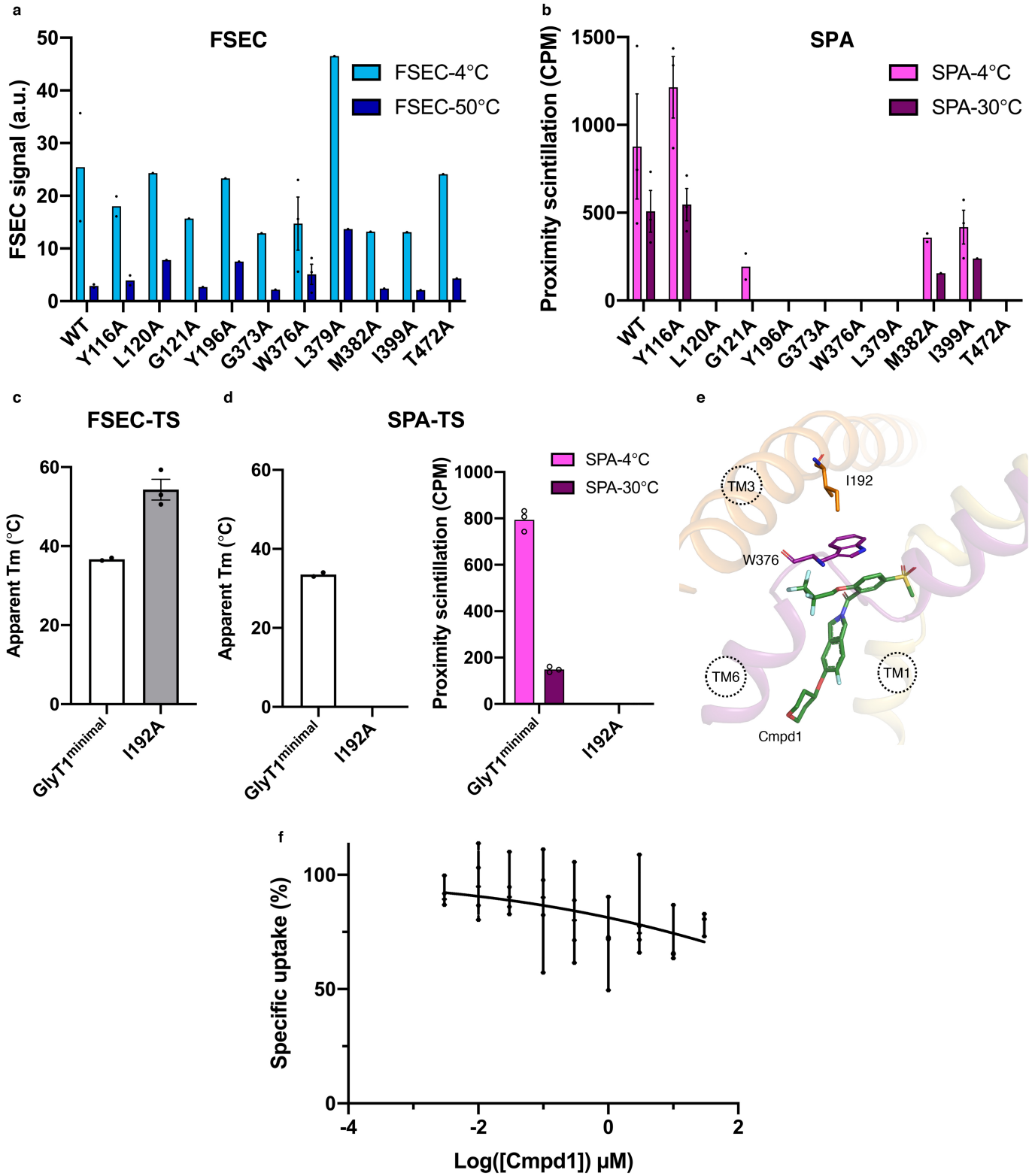

Extended Data Fig. 6 | See next page for caption.

Extended Data Fig. 6 | Effects of single mutations in residues of the inhibitor-binding pocket of GlyT1, and selectivity of Cmpd1 against GlyT2. **a**, **b**, FSEC (**a**) and SPA (**b**) signals measured for single-mutation constructs of GlyT1 compared with the wild-type transporter at 4 °C and 50 °C (**a**) or 4 °C and 30 °C (**b**). The absence of an SPA signal for the L120A, Y196A, G373A, W376A, L379A and T472A constructs confirms the inability of the mutant to bind the inhibitor. A weak SPA signal for the G121A construct at 4 °C, and for the M382A and I399A constructs at both 4 °C and 30 °C, was measured. A relatively higher SPA signal for the Y116A mutant can be explained as the isoindoline scaffold of the inhibitor is further supported by hydrophobic interactions with surrounding residues other than Y116. Bars represent average FSEC and SPA signals in **a** and **b**, respectively (in **a**, shown are individual data points from $n = 3$ independent experiments for W376A, $n = 2$ for wild-type and Y116A, and $n = 1$ for L120A, G121A, Y196A, G373A, L379A, M382A, I399A and T472A; in **b**, from $n = 3$ for wild-type, Y116A, and I399A, $n = 2$ for G121A, G373A, W376A and M382A, and $n = 1$ for L120A, Y196A, L379A and T472A; each in $n = 3$ technical replicates). Error bars represent s.e.m. **c**, Thermostabilizing effect of the I192A mutation (introduced into the GlyT1^{minimal} construct, which also contains N- and C-terminal deletions of residues 1–90 and 685–706) compared with GlyT1^{minimal}, measured by FSEC–TS analysis. Apparent T_m values for GlyT1^{minimal} and the I192A mutant were 36.6 ± 0.5 °C and 52.5 ± 1.5 °C, respectively. Bars represent average apparent T_m values, with data points from $n = 2$ and $n = 3$ independent experiments for GlyT1^{minimal} and I192A, respectively, shown as individual circles (±s.e.m.). **d**, Nonbinding I192A mutation. Left, a comparable (with the value obtained by FSEC–TS analysis) apparent T_m value of 33.5 ± 0.4 °C was measured for GlyT1^{minimal} in SPA–TS analysis, while no signal was observed for the I192A mutant (left, $n = 2$ independent experiments, each with triplicate measurements; shown are means ± s.e.m.). Right, SPA signals measured at 4 °C and 30 °C. The absence of a signal for I192A confirms the inability of the mutant to bind the inhibitor. Bars represent the average SPA signal, with individual data points from $n = 3$ technical replicates shown. The experiment was repeated independently once with similar results. **e**, Position of I192A (in TM3), stabilizing a rotamer of W376 (TM6) in an edge-to-face stacking interaction with Cmpd1. **f**, Assay for [^{3}H]glycine-uptake inhibition in mammalian Flp-in-CHO cells transfected with human GlyT2 cDNA, showing that Cmpd1, a selective inhibitor of GlyT1, does not inhibit uptake of glycine by GlyT2. The curve was calculated from $n = 4$ technical replicates (individual data points are shown; whiskers extend from minimum to maximum).

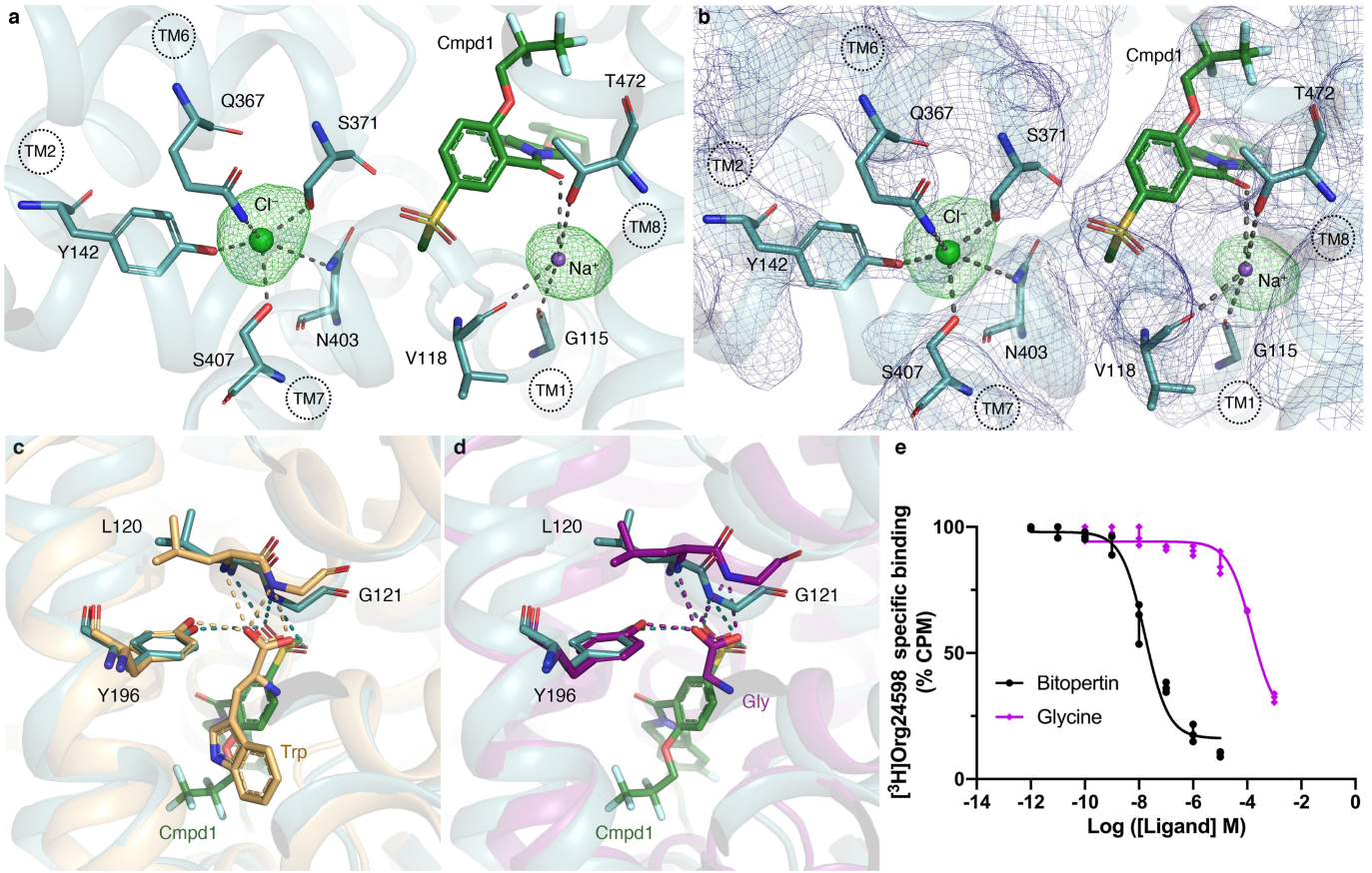

Extended Data Fig. 7 | Ion- and glycine-binding sites in GlyT1. a, Cl^- (light green) and Na^+ (purple) ions in the GlyT1–Lic structure are shown as spheres. $F_o - F_c$ simulated annealing composite omit maps (green mesh) for Cl^- and Na^+ ions (prominent peaks at 6.8 r.m.s.d. and 6.5 r.m.s.d., respectively, in an unbiased difference map, chain A) are shown at 4.0 r.m.s.d. Cmpd1 is depicted in green and the residues that are likely to coordinate the Cl^- and Na^+ ions are shown as sticks and with dashed lines (chain A in the asymmetric unit). The Cl^- ion is coordinated by conserved residues Y142 (TM2), Q367 (TM6), S371 (in the unwound region of TM6) and S407 (TM7), similar to the Cl^- site in dDAT and SERT[18,22], with a mean coordination distance of 3.0 Å, and probably also by N403 (TM7)[60], but with a longer coordination distance. Mutation of residues Q367 and S407 has further been shown to affect GlyT1's response to Cl^-, highlighting the involvement of these residues in Cl^- binding[61].The Na^+ ion in the Na2 site is within a mean coordination distance of 3.1 Å from the carbonyl oxygen of the conserved residues G115, V118 (TM1) and T472 (TM8), as observed in previous structures of NSS transporters, and the carbonyl oxygen of the Cmpd1 scaffold (measured in chain A of the asymmetric unit). The Na1 site observed in other NSS structures is occupied by the methyl sulfone substituent of the inhibitor in this structure. **b**, The $2F_o - F_c$ electron density map (blue) for helices involved in ion binding is contoured at 1.0 r.m.s.d. **c**, **d**, Superposition of tryptophan-bound MhsT (**c**; light orange, PDB ID 4US3; ref. [17]) and glycine-bound LeuT (**d**; purple, PDB ID 3F4J; ref. [62]) on Cmpd1-bound GlyT1 (cyan). The sulfonyl moiety of the inhibitor matches with the carboxylate of tryptophan or glycine. Glycine bound to GlyT1 probably interacts with the backbone amide of L120 and G121 from TM1 and the hydroxyl group of Y196 from TM3, similar to the stabilizing interactions of LeuT and MhsT with their respective bound ligands, glycine and tryptophan. **d**, Scintillation proximity competition assays using [^{3}H]Org24598 and varying concentrations of bitopertin and glycine with $GlyT1^{minimal}$, showing that bitopertin and glycine compete with [^{3}H]Org24598 at concentrations of $1.0 \times 10^{-5} \pm 1.8 \times 10^{-6}$ mM and 0.1 ± 0.003 mM (means ± s.e.m. from triplicate measurements), respectively. Although direct competition between bitopertin and glycine is not shown in the experiment, the similarities of [^{3}H]Org24598/bitopertin are nevertheless highly suggestive that bitopertin and glycine also compete with each other for binding at GlyT1. Curves were calculated from $n = 3$ technical replicates (individual measurements are shown; whiskers extend from minimum to maximum).

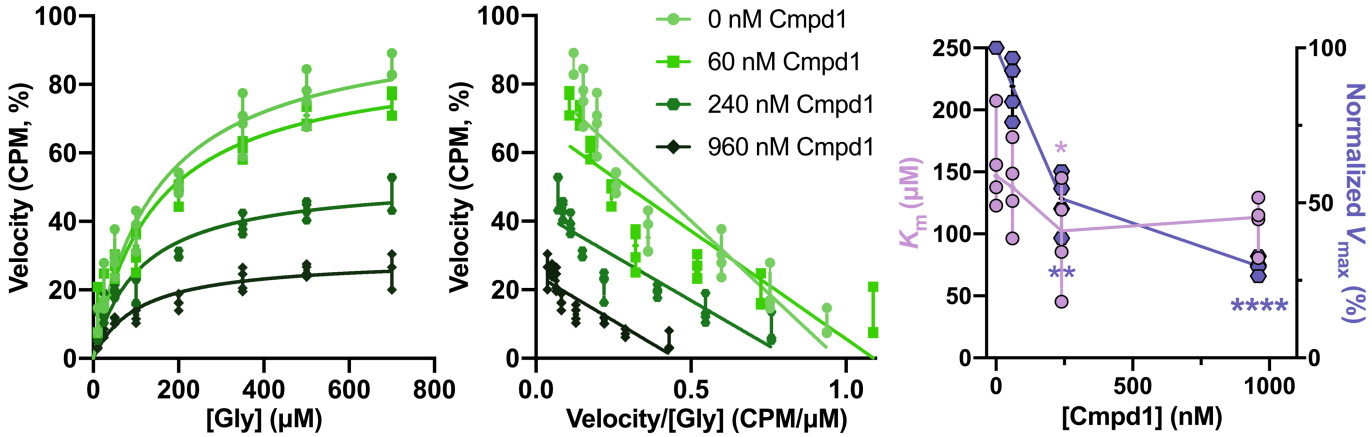

Extended Data Fig. 8 | Inhibition of GlyT1-mediated glycine transport by Cmpd1 is not competitive. Left, uptake assays using HEK293-MSR cells transfected with $GlyT1^{wt}$ display Michaelis–Menten kinetics that can be inhibited by Cmpd1 in a dose-dependent manner. Centre, Eadie–Hofstee plots of uptake data verify that the inhibition of GlyT1-mediated glycine uptake by Cmpd1 is not competitive (independent experiments are normalized against V_{max}). Right, kinetic parameters derived from Michaelis–Menten analysis show that Cmpd1 reduces V_{max} (normalized representation) in a dose-dependent manner ($P = 0.0038$ and $P < 0.0001$ for V_{max} at 240 nM and 960 nM of Cmpd1, respectively), whereas K_m values are mostly not altered by increasing the inhibitor concentration, except for a single concentration ($P = 0.0152$ at 240 nM of Cmpd1). K_m and V_{max} values for increasing concentrations of Cmpd1 are 156 ± 18 μM, 137 ± 17 μM, 99 ± 22 μM and 109 ± 10 μM, and 18,564 ± 3,381 CPM, 16,524 ± 3534 CPM, 9,819 ± 2,437 CPM and 5,512 ± 1,076 CPM, respectively (means ± s.e.m.). These data exclude competitive inhibition for the inhibitor. Curves were calculated from $n = 4$ independent experiments, each performed with duplicate measurements. Data points are the average of independent experiments. Whiskers extend from minimum to maximum. One-way analysis of variance (ANOVA), corrected according to Dunnett's test, was used to determine whether each mean of aggregate data from four independent experiments was significantly different from the corresponding value with no inhibitor present (****$P < 0.0001$; **$P < 0.01$; *$P < 0.05$).

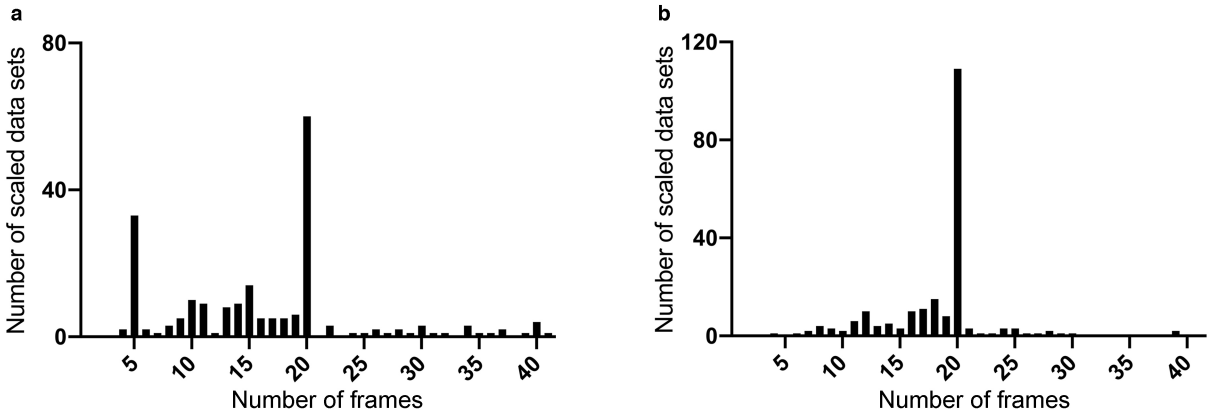

c

Resolution Limit (Å)	Number of Reflections Observed	Unique	Possible	Completeness	R-Factor Observed	I/Sigma	R-meas	CC(1/2)
25.0	183	30	31	96.8%	10.0%	15.99	10.9%	99.3
15.0	1445	221	222	99.5%	11.8%	17.59	12.8%	99.1
10.0	4595	670	675	99.3%	12.7%	16.15	13.8%	98.9
5.0	20247	3177	3211	98.9%	44.6%	5.19	48.6%	89.3
4.0	46129	7219	7283	99.1%	61.0%	4.41	66.3%	84.5
3.8	8249	1297	1311	98.9%	127.8%	2.16	139.1%	51.2
3.7	9129	1446	1445	100.0%	145.5%	1.74	158.3%	49.3
3.6	9726	1582	1606	98.5%	153.2%	1.50	167.3%	46.7
3.5	11305	1802	1809	99.6%	197.2%	1.29	215.0%	44.7
3.4	7500	1217	1227	99.2%	299.2%	0.94	326.4%	30.1
Total	153451	24071	24304	99.0%	41.5%	4.36	45.1%	97.5

d

Resolution Limit (Å)	Number of Reflections Observed	Unique	Possible	Completeness	R-Factor Observed	I/Sigma	R-meas	CC(1/2)
25.0	515	42	42	100.0%	11.9%	23.98	12.5%	100.0
15.0	4268	326	327	99.7%	13.9%	20.11	14.5%	99.8
10.0	13736	976	975	100.0%	16.9%	19.27	17.6%	99.5
8.0	18010	1291	1291	100.0%	23.5	13.85	24.4%	99.3
5.0	112156	7979	7980	100.0%	92.4%	4.35	95.9%	91.7
4.8	19359	1402	1402	100.0%	147.0%	2.79	152.7%	84.2
4.6	22569	1618	1619	99.9%	177.5%	2.43	184.4%	79.1
4.4	26270	1901	1899	100.0%	173.6%	2.19	180.3%	73.5
4.2	32001	2309	2309	100.0%	294.4%	1.48	305.7%	63.4
4.0	37805	2784	2784	100.0%	460.3%	1.00	478.5%	42.1
3.9	21006	1606	1606	100.0%	656.4%	0.77	683.4%	29.4
Total	307695	22234	22296	99.7%	92.1%	4.42	95.7%	98.5

Extended Data Fig. 9 | Number of scaled mini datasets per number of frames, and statistics of scaled mini datasets for GlyT1 and GlyT1–Lic crystals. a, **c**, GlyT1; **b**, **d**, GlyT1–Lic. **a**, **b**, Numbers of scaled partial datasets with a given number of frames (1–41) for GlyT1 (**a**) and GlyT1–Lic (**b**) datasets. Mini datasets containing 3–20 frames were picked automatically; in several cases, mini datasets adjacent in frame numbers were manually merged into larger datasets containing more than 20 frames. **c**, **d**, Statistics of scaled mini datasets for GlyT1 (**c**) and GlyT1–Lic (**d**). Calculated by XSCALE[45], *I*/Sigma is the mean of the reflection intensity, *I*, of unique reflections divided by the standard deviation of the reflection intensity, after merging symmetry-related observations. R-meas is the redundancy-independent R-factor (for intensities)[63]. CC(1/2) is the percentage of correlation between intensities from random half-datasets[64].

Extended Data Table 1 | Data collection and refinement statistics

	GlyT1 † (PDB ID 6ZBV)	GlyT1-Lic ‡ (PDB ID 6ZPL)
Data collection	$P2_1$	$P2_1$
Space group		
Cell dimensions		
a, *b*, *c* (Å)	65.17, 58.14, 122.31	116.41, 69.71, 149.43
α, β, γ (°)	90.00, 100.38, 90.00	90.00, 92.86, 90.00
Resolution (Å)	29.7 - 3.4 (3.5 - 3.4) *	29.3 - 3.9 (4.04 - 3.90)
R_{merge} (%)	42.2 (268.8)	85.9 (542.6)
$I / \sigma I$	6.5 (1.6)	4.2 (1.0)
CC1/2	98.9 (54.1)	98.0 (28.6)
Completeness (%)	99.7 (100.0)	99.6 (99.9)
Redundancy	12.1 (11.9)	12.7 (12.2)
Refinement		
Resolution (Å)	29.7 - 3.4 (3.5 - 3.4)	29.070 - 3.945 (4.086 - 3.945)
No. reflections	153292 (14642)	272064 (25894)
R_{work} / R_{free} (%)	21.5/25.8 (21.0/26.4)	27.7/29.1 (21.5/31.5)
No. atoms		
Protein	5222	12413
Ligand/ion	38/0	76/4
Water	0	0
B-factors		
Protein	103.2	91.7
Ligand/ion	118.2	97.9/63.4
Water		
R.m.s. deviations		
Bond lengths (Å)	0.011	0.011
Bond angles (°)	1.67	1.51

Statistics on data collection were calculated using Phenix[49].
*Values in parentheses are for the highest-resolution shell.
†Data merged from 409 mounted loops containing microcrystals.
‡Data merged from 1,222 mounted loops containing microcrystals.

nature research

Corresponding author(s): Thomas R. Schneider, Roger J.P. Dawson, Poul Nissen

Last updated by author(s): Jan 5, 2021

Reporting Summary

Nature Research wishes to improve the reproducibility of the work that we publish. This form provides structure for consistency and transparency in reporting. For further information on Nature Research policies, see our Editorial Policies and the Editorial Policy Checklist.

Statistics

For all statistical analyses, confirm that the following items are present in the figure legend, table legend, main text, or Methods section.

n/a	Confirmed	
☐	☒	The exact sample size (*n*) for each experimental group/condition, given as a discrete number and unit of measurement
☐	☒	A statement on whether measurements were taken from distinct samples or whether the same sample was measured repeatedly
☐	☒	The statistical test(s) used AND whether they are one- or two-sided *Only common tests should be described solely by name; describe more complex techniques in the Methods section.*
☒	☐	A description of all covariates tested
☐	☒	A description of any assumptions or corrections, such as tests of normality and adjustment for multiple comparisons
☐	☒	A full description of the statistical parameters including central tendency (e.g. means) or other basic estimates (e.g. regression coefficient) AND variation (e.g. standard deviation) or associated estimates of uncertainty (e.g. confidence intervals)
☐	☒	For null hypothesis testing, the test statistic (e.g. *F*, *t*, *r*) with confidence intervals, effect sizes, degrees of freedom and *P* value noted *Give P values as exact values whenever suitable.*
☒	☐	For Bayesian analysis, information on the choice of priors and Markov chain Monte Carlo settings
☒	☐	For hierarchical and complex designs, identification of the appropriate level for tests and full reporting of outcomes
☒	☐	Estimates of effect sizes (e.g. Cohen's *d*, Pearson's *r*), indicating how they were calculated

Our web collection on statistics for biologists contains articles on many of the points above.

Software and code

Policy information about availability of computer code

Data collection	Serial synchrotron crystallographic data were collected at P14 beamline operated by EMBL Hamburg at the PETRA III storage ring (DESY, Hamburg).
Data analysis	Diffraction data was indexed and integrated using XDS and scaled with XSCALE, versions January 26, 2018 BUILT=20180808 and March 15, 2019 BUILT=20190606. Ctrl-d 0.3.465 was used to measure the correlation of each mini data set to the rest of mini data sets. The executable Ctrl-d is available via webapps.embl-hamburg.de. Molecular replacement was performed using Phaser versions 2.8.2 and 2.8.3 as implemented in Phenix 1.14-3260 and 1.17.1-3660, respectively. Model building was performed using Coot 0.8 and ISOLDE 0.93. The models were refined using Buster 2.10.3. Contact from ccp4 program suit 7.0 was used to analyze the interface of macromolecules. OpenEye molecular modeling Toolkit 2020.1.1 was used to generate 3D conformers (Omega) and superimpose the conformers (ROCS). MOE 2019.01 was used for energy minimization of the conformers and calculating the protein-ligand interactions diagram. Docking was performed with the software GOLD from 2020.1 CSD Release version as implemented in CCDC 2020.1. Protein structure figures were prepared using PyMOL 2.3.3 - Incentive Product, Schrodinger, LLC. Sequences were aligned using ClustalOmega (https://www.ebi.ac.uk/Tools/msa/clustalo/) and figure was prepared using BOXSHADE 3.2. Binding and uptake data were analyzed and figures prepared using GraphPad Prism version 9. All of the software is published and referenced in the Extended Data section. All but OpenEye, MOE, CCDC , PyMOL and GraphPad Prism are open source.

For manuscripts utilizing custom algorithms or software that are central to the research but not yet described in published literature, software must be made available to editors and reviewers. We strongly encourage code deposition in a community repository (e.g. GitHub). See the Nature Research guidelines for submitting code & software for further information.

Data

Policy information about availability of data

All manuscripts must include a data availability statement. This statement should provide the following information, where applicable:

- Accession codes, unique identifiers, or web links for publicly available datasets
- A list of figures that have associated raw data
- A description of any restrictions on data availability

Coordinates and structure factors of 3.4 Å and 3.9 Å resolution structures of GlyT1 have been deposited in the Protein Data Bank under accession codes 6ZBV and 6ZPL, respectively. The executable Ctrl-d is available via webapps.embl-hamburg.de.

Field-specific reporting

Please select the one below that is the best fit for your research. If you are not sure, read the appropriate sections before making your selection.

☒ Life sciences ☐ Behavioural & social sciences ☐ Ecological, evolutionary & environmental sciences

For a reference copy of the document with all sections, see nature.com/documents/nr-reporting-summary-flat.pdf

Life sciences study design

All studies must disclose on these points even when the disclosure is negative.

Sample size	No statistical methods were used to predetermine sample size. The determined sample size was adequate based on the overall distribution of data points and clearly visible effects and as the differences between experimental groups was reproducible, as indicated. X-ray diffraction data were collected until completeness of the data sets with multiplicity of above 5.
Data exclusions	No data were excluded to plot results displayed in any figures or tables.
Replication	The experimental findings were reproduced in independent experiments or technical replicates. The number of independent experiments and technical replicates in each data panel is indicated in the figure legends. All experiments were reproducible.
Randomization	No group allocation was performed in this study.
Blinding	Authors were not blinded and no blinding was attempted or needed. Blinding is not relevant for protein structure determination or biochemical and functional assays as the results are not subjective.

Reporting for specific materials, systems and methods

We require information from authors about some types of materials, experimental systems and methods used in many studies. Here, indicate whether each material, system or method listed is relevant to your study. If you are not sure if a list item applies to your research, read the appropriate section before selecting a response.

Materials & experimental systems

n/a	Involved in the study
☐	☒ Antibodies
☐	☒ Eukaryotic cell lines
☒	☐ Palaeontology and archaeology
☒	☐ Animals and other organisms
☒	☐ Human research participants
☒	☐ Clinical data
☒	☐ Dual use research of concern

Methods

n/a	Involved in the study
☒	☐ ChIP-seq
☒	☐ Flow cytometry
☒	☐ MRI-based neuroimaging

Antibodies

Antibodies used	Synthetic single domain antibody, sybody Sb_GlyT1#7 (Zimmermann et al. (2018) eLife.34317.001)
Validation	Validation of the sybody has been described in Zimmermann et al. (2018) eLife.34317.001 and Zimmermann et al. (2020) Nat Protoc 15, 1707–1741.

Eukaryotic cell lines

Policy information about cell lines

Cell line source(s)	Human embryonic kidney (HEK293) cells (Invitrogen), HEK293-MSR cells (Invitrogen), Spodoptera frugiperda (Sf9) insect cells (ATCC® CRL-1711™), Flp-in™-CHO cells (Invitrogen) and Escherichia coli MC1061.
Authentication	Spodoptera frugiperda (Sf9) insect cells and Flp-in™-CHO cells were authenticated. Human embryonic kidney (HEK293) cells and HEK293-MSR cells were not authenticated.
Mycoplasma contamination	Spodoptera frugiperda (Sf9) insect cells and Flp-in™-CHO cells were free of mycoplasma contamination. Human embryonic kidney (HEK293) cells and HEK293-MSR cells were not tested for mycoplasma contamination.
Commonly misidentified lines (See ICLAC register)	No commonly misidentified cell lines were used.